$^{14}C(n,\gamma)^{15}C$ AS A TEST CASE IN THE EVALUATION OF A NEW METHOD TO DETERMINE SPECTROSCOPIC FACTORS USING ASYMPTOTIC NORMALIZATION COEFFICIENTS

A Dissertation

by

MATTHEW EDGAR M^{C}CLESKEY

Submitted to the Office of Graduate Studies of
Texas A&M University
in partial fulfillment of the requirements for the degree of

DOCTOR OF PHILOSOPHY

December 2011

Major Subject: Physics

$^{14}C(n,\gamma)^{15}C$ AS A TEST CASE IN THE EVALUATION OF A NEW METHOD TO DETERMINE SPECTROSCOPIC FACTORS USING ASYMPTOTIC NORMALIZATION COEFFICIENTS

A Dissertation

by

MATTHEW EDGAR M^{C}CLESKEY

Submitted to the Office of Graduate Studies of
Texas A&M University
in partial fulfillment of the requirements for the degree of

DOCTOR OF PHILOSOPHY

Approved by:

Chair of Committee,	Robert E. Tribble
Committee Members,	Carl A. Gagliardi
	Dan Melconian
	Joseph B. Natowitz
Head of Department,	Edward Fry

December 2011

Major Subject: Physics

ABSTRACT

$^{14}C(n,\gamma)^{15}C$ as a Test Case in the Evaluation of a New Method to Determine Spectroscopic Factors Using Asymptotic Normalization Coefficients.

(December 2011)

Matthew Edgar McCleskey, B.S., Texas A&M University

Chair of Advisory Committee: Dr. Robert E. Tribble

With new radioactive isotope accelerators coming online in the next decade, the problem of extracting reliable nuclear structure information from reactions with unstable nuclei deserves considerable attention. A method has been proposed to determine spectroscopic factors (SFs) using the asymptotic normalization coefficient (ANC) to fix the external contribution of a non-peripheral reaction, reducing the uncertainty in the SF. The $^{15}C\leftrightarrow^{14}C+n$ system was chosen as a test case for this new method. The direct neutron capture rate on ^{14}C is important for a variety of topics of interest in astrophysics, and the ANC for $^{15}C\leftrightarrow^{14}C+n$ was also used to calculate this reaction rate.

The objective of the first part of this work was to find the ANC for $^{15}C\leftrightarrow^{14}C+n$. This was done in two independent experiments. First, the heavy ion neutron transfer reaction $^{13}C(^{14}C,^{15}C)^{12}C$ was measured at 12 MeV/nucleon. Second, the inverse kinematics reaction $d(^{14}C,p)^{15}C$ was measured using the new Texas Edinburgh Catania Silicon Array (TECSA). The next phase of the experimental program was to measure a reaction with a non-negligible interior contribution, for which $^{14}C(d,p)^{15}C$ at 60 MeV deuteron energy was used. This reaction turned out to be more peripheral than anticipated, and as a result, the ANC for the ground state was extracted from this measurement as well. The final results for the three measurements are $C^2_{2s_{1/2}} = 1.96\pm0.16$ fm^{-1} for the ground state and $C^2_{1d_{5/2}} = (4.23\pm0.38)\cdot10^{-3}$ fm^{-1} for the first excited state.

Because the 60 MeV $^{14}C(d,p)^{15}C$ reaction turned out to have a very weak dependence on the interior, the SF could not be determined for the $^{14}C+n$ ground state in ^{15}C using the new method. A lower limit of 1.05 was found for the first excited state. It is possible that other reactions might turn out to be more suitable for this method, however, the difficulty encountered

at this relatively high deuteron energy highlights a substantial problem likely to be seen in other applications.

Using the ANCs determined in this work, the astrophysical $^{14}C(n,\gamma)^{15}C$ reaction rate was calculated. The resulting value for the cross section for capture to the ground state at 23 keV was $\sigma_{gs}(23\ keV)=5.1\pm0.4\ \mu b$ and to the first excited state was $\sigma_{exc}(23\ keV)=0.2\pm0.02\ \mu b$.

To Mr. Barry Rose

ACKNOWLEDGEMENTS

I am grateful to have had this chance to study at the Cyclotron Institute at Texas A&M University. Few places could offer the opportunities, support and guidance that I have found here. I would like to thank my advisor, Prof. Robert Tribble, for all of his input and help on this project and in general over the years. Also, I would like to thank Dr. Mukhamedzhanov, who is responsible for the theoretical work upon which this work is based, for his time and effort in explaining the theory to me and discussing my results.

Dr. Livius Trache has been a great mentor and teacher, and it has truly been a pleasure to work with him. I am indebted to him for his countless hours and great patience in answering my questions, and for his input on this work and the other projects I have been involved with while here.

Additionally, I would like to thank my committee members, Prof. Gagliardi, Prof. Melconian and Prof. Natowitz, for their time, input and suggestions. A similar note of thanks is extended to Dr. V. Goldberg for many useful discussions.

I must express my sincere appreciation for the work of Prof. Florin Carstoiu on the analysis of the heavy ion elastic scattering. Also, I would like to thank Ngoc Nguyen for her help with the adiabatic distorted wave approximation (ADWA) calculations and for providing me with her FRESCO input files. Additionally, I would like to acknowledge Prof. J. Tostevin for his input regarding the ADWA potentials.

I would also like to thank the members of the RET group for their help with these measurements, specifically Prof. T. Al-Abdullah, Prof. A. Alharby, Prof. A. Banu, Dr. B. Roeder and Ms. A. Spiridon. Additionally, I must thank the DHY group for their contributions and assistance with the measurements on the multipole-dipole-multipole (MDM) spectrometer, in particular Dr. Y.-W. Lui, Dr. X. Chen, Dr. Krishichayan and Mr. J. Button. A special note of appreciation is due to Ms. E. Simmons, not only for her substantial contributions to the measurements presented here, but for her love and support throughout this process.

I would like to thank the TECSA collaboration whose efforts made possible the successful d(^{14}C,p)^{15}C measurement as the commissioning run of TECSA. I must also thank our collaborators at the Nuclear Physics Institute of the Czech Academy of the Sciences, in

particular Dr. V. Burjan, Dr. V. Kroha, and Dr. Z. Hons, for their contributions to the $^{14}C(d,p)^{15}C$ measurement.

None of these measurements would be possible without the excellent support staff at the Texas A&M Cyclotron. In particular, I would like to thank Mr. L. Norris, Mr. L. Whitley, Mr. A. Clark, Mr. J. Raines, and Mr. S. Molitor for their help and input on the TECSA project, as well as many other projects over the years.

Finally, I would like to express my gratitude for the NNSA Stockpile Stewardship Academic Alliance for funding this work.

TABLE OF CONTENTS

LIST OF FIGURES

Page

Page

LIST OF TABLES

CHAPTER I

INTRODUCTION

It was only a century ago that the existence of the atomic nucleus as we now know it was discovered by Earnest Rutherford [1] based on his now famous scattering experiments. The magnitude of this discovery is perhaps best captured by Rutherford himself [2]:

> It was quite the most incredible event that has ever happened to me in my life. It was almost as incredible as if you fired a 15-inch shell at a piece of tissue paper and it came back and hit you. On consideration, I realized that this scattering backward must be the result of a single collision, and when I made calculations I saw that it was impossible to get anything of that order of magnitude unless you took a system in which the greater part of the mass of the atom was concentrated in a minute nucleus. It was then that I had the idea of an atom with a minute massive centre, carrying a charge.

Prevailing ideas of matter at that time had the mass and charge of the atom spread throughout its volume, yet what Rutherford had found from his examination of scattering data was something entirely different: a compact, positively charged nucleus that would have to be held together by a force great enough to overcome the significant Coulomb repulsion that would take place at such small distances. This insight was, in a sense, our first step towards the body of knowledge upon which we now stand as we peer into distant galaxies and contemplate the inner workings of stars and novae. Our study of the nucleus and nuclear reactions has had a profound effect for mankind in everything from our terrestrial concerns such as energy, security, and medicine to providing some of the answers to basic questions such as the origin of elements from which the first stars were made.

When a nucleon (or another nucleus) collides with a nucleus many types of interactions are possible. The simplest interaction would be elastic scattering like that observed by Rutherford. Alternatively, a reaction could take place which changes the nucleus. The concept of compound nucleus formation to describe reactions between nuclei was formulated in the 1930's [3]. In a compound nuclear reaction the projectile is absorbed into the target nucleus and has many interactions with the constituent parts of the target. The resulting excited

---

This dissertation follows the format of Physical Review C.

compound nucleus, through these many complex interactions, loses essentially all information about how it was formed, and because the energy of the incident particle is distributed amongst so many constituent nucleons of the target, the energy of each one is low as is the probability of one escaping. As a result, compound nuclear reactions are characterized by time durations much longer than the time it would take for the projectile to simply traverse the nucleus, also, the angular distribution of reaction products is isotropic, which is consistent with a compound system that has "forgotten" the input channel. This has been exploited to indirectly study (n,γ) and (n,f) reactions via other reactions such as A(d,p)B* using the so-called surrogate method (see, for example, [4]).

In contrast to compound nuclear reactions, direct reactions take place on time scales comparable to that which it would take for the projectile to pass through the nucleus. Only a single interaction occurs inside the nucleus and the angular distributions are forward-peaked. Indeed, the reaction may not take place inside the nucleus at all, but rather in the surface region, maybe interacting with a single valence nucleon in a shell model orbital. Because of this, direct reactions were recognized early on as a means to probe the single particle structure of the nuclear states involved in the reaction. Specifically, it was shown by Butler [5] that (d,p) and (d,n) reactions were strongly dependent on the spins and parities of the nuclei involved in the reaction, and that the spin and parity of one state could be determined if the other was known based on the shape of the angular distribution of ejectile.

In the decades following the theoretical description of Butler and others of direct nuclear reactions, many measurements were made and many different models were proposed and developed to understand nuclei. Much was learned. However, the recent development of radioactive beam facilities around the world, capable of providing beams of nuclei far from stability that are now, in many cases, high enough in kinetic energy and intensity to study reactions, has fostered a nuclear renaissance. Methods to extract reliable nuclear structure information from reactions with available unstable nuclei need to continue to be developed and improved upon.

In particular, neutron capture reactions on unstable nuclei present a challenging problem for nuclear physics. Their cross sections are needed for a variety of applications. However, due to practical considerations, direct measurements are difficult if not impossible. Inverse kinematics, as is often used for reactions involving unstable particles, is not available as no neutron target exists. While forward kinematics may be an option for neutron capture on either

stable or long-lived targets, capture on very short-lived radioactive nuclei cannot be measured in this way as making a target of such an unstable isotope is not possible. It is therefore imperative that indirect methods for determining these capture cross sections be developed.

Indirect methods for determining reaction cross sections generally involve making a laboratory measurement of a relevant physical quantity that can then be related to the reaction of interest by means of knowledge of the nuclear structure. Traditionally this has taken the form of the measurement of angular distributions of transfer reactions at laboratory energies that are then analyzed using the distorted-wave Born approximation (DWBA) for the purpose of extracting the spectroscopic factors (SFs), often taken as the ratio of the experimental angular distribution to that of a DWBA calculation. A SF determined in this way is model-dependent and the usefulness of such a number is limited as it is only meaningful with detailed knowledge of the DWBA calculation that was performed and the potentials and wave functions used.

A. ANCs and a new method for extracting SFs

The asymptotic normalization coefficient (ANC) is the factor which determines the normalization of the tail of the radial overlap function at large radii [6]. At these large radii the overlap function behaves as a Whittaker function or, in the case of a neutron being transferred, a Hankel function of the first kind. The traditional form of parameterizing the experimentally measured angular distribution to the calculated distribution in terms of the SFs is

$$\left(\frac{d\sigma(\theta)}{d\Omega}\right)_{exp} = \sum_{j_B j_a} S_{Axl_B j_B} S_{bxl_a j_a} \sigma^{DW}_{l_B j_B l_a j_a}, \tag{1.1}$$

where the transfer of a nucleon x from an incoming projectile $a = b + x$ onto a target nucleus A to form the final nucleus $B = A + x$ is considered. The SF $S_{bxl_a j_a}$ can be thought of as the probability for finding the configuration of the particle x in a single particle shell model orbital $l_a j_a$ in a moving about the core b, which is in its ground state. This common shell model interpretation of the SF does not hold if the radial overlap function differs significantly from the single particle bound state wave function [7], which may very well be the case particularly in the interior of the nucleus.

Most transfer reactions between charged particles measured in the laboratory at reasonably low energies are largely peripheral. As such, they may not probe the nuclear interior at all and thus give no information about the behavior of the radial overlap function in the

interior. In these situations the parameterization of (1.1) will not be meaningful as the calculation of $\sigma^{DW}_{l_B j_B l_a j_a}$ will be strongly dependent on the choice of the bound state potential geometry, which is chosen based on standard values which give reasonable results for many reactions. A more relevant quantity in such a situation is the ANC which can be experimentally determined in peripheral reactions using a parameterization analogous to (1.1), namely

$$\frac{d\sigma}{d\Omega} = \sum_{j_B l_B} (C^B_{Axl_B j_B})^2 (C^a_{bxl_a j_a})^2 \frac{\sigma^{DW}_{l_B j_B l_a j_a}}{b^2_{Axl_B j_B} b^2_{bxl_a j_a}}. \tag{1.2}$$

Here b is the single particle ANC (SPANC) for the configurations $A + x$ in B and $b + x$ in a. The SPANC contains the dependence on the binding potential and this parameter dependence is canceled out in the ratio

$$\frac{\sigma^{DW}_{l_B j_B l_a j_a}}{b^2_{Axl_B j_B} b^2_{bxl_a j_a}}. \tag{1.3}$$

The ANCs extracted via (1.2) for a peripheral reaction are therefore a more parameter independent quantity than the SFs of (1.1). Since many reactions of significance to stellar evolution, such as all low energy proton capture and even some neutron capture reactions, are peripheral processes, the ANC is very useful for determining these rates [8], [9].

A new method to extract spectroscopic factors utilizing asymptotic normalization coefficients (ANCs) has been proposed [8]. The details of the approach will be given in Chapter II, but the basic idea is to use two reactions, the first peripheral to determine the relevant ANC and a second reaction that is non-peripheral to find the SF. The SF is determined by using the ANC to fix the external part of the DWBA amplitude and then varying the bound state geometry to give the DWBA amplitude as a function of the SPANC. By doing this, the SPANC can be fixed experimentally giving the correct SF by

$$S_{lj} = \frac{C^2_{lj}}{b^2_{lj}}. \tag{1.4}$$

This approach requires for the second reaction one that both has a significant contribution from the interior but also is described well under the DWBA, the assumptions of which will also be described in Chapter II.

^{15}C has been chosen as a test case for this procedure. It is a loosely bound neutron-rich nucleus which should be described well in the single particle approximation and has been well studied due to the astrophysical interest in the ^{14}C(n,γ)^{15}C reaction, which will be discussed in

the next section. This reaction is one of the few neutron capture reactions on unstable nuclei that has both been measured directly and for which numerous indirect determinations of the cross section exist. Despite this, however, a significant disagreement in the cross section has persisted for close to 20 years, and only recently have the various determinations started to come into agreement. As such, a good determination of the ANC for $^{15}C \leftrightarrow ^{14}C+n$ is desirable as a means to independently calculate the neutron capture cross section at astrophysical energies, which is possible since it is a peripheral capture process [10]. This ANC has been determined previously ([11], [12], [13], [14]) however the current numbers are not in good agreement and a new independent determination is desirable.

B. $^{14}C(n,\gamma)^{15}C$

The neutron capture on ^{14}C is an important reaction for nuclear astrophysics both because of the important role it plays in several astrophysical processes and because it is one of the few reactions where it is possible to validate indirect methods against direct measurements for neutron capture cross sections [10]. Several indirect methods have been applied to this reaction such as Coulomb dissociation, nuclear breakup, and the ANC approach.

Inhomogeneous big bang nucleosynthesis (BBN) was proposed [15] as a mechanism by which neutron-rich regions could be formed in the early universe [16]. These regions could give rise to the production of heavier elements than what could be expected by standard BBN and thus potentially answer some outstanding questions about the presence of metals (nuclei heavier than helium) in the earliest observed stars. It should be noted, however, that inhomogeneous BBN is not widely accepted and it has been argued [17] that any such inhomogeneities would have little impact on heavy element abundances if observational constraints such as ^{7}Li abundance are imposed on the model. Nevertheless, there is a continued interest in the topic and if such regions do occur, the reaction chain

$$^{7}\mathrm{Li}(n,\gamma)\,^{8}\mathrm{Li}(\alpha,n)\,^{11}\mathrm{B}(n,\gamma)\,^{12}\mathrm{B}(\beta)\,^{12}\mathrm{C}(n,\gamma)\,^{13}\mathrm{C}(n,\gamma)\,^{14}\mathrm{C}$$

may contribute to the production of A>12 nuclei. Since this chain ends at the long lived ^{14}C ($t_{1/2}$ ~ 6000 y, stable on the timescale of BBN) subsequent reactions on ^{14}C could have an impact on the production of heavier elements [16].

Another astrophysical scenario in which the cross section for $^{14}C(n,\gamma)$ is important is in the neutron-induced depletion of carbon-nitrogen-oxygen (CNO) cycle isotopes in the helium

burning layer of asymptotic giant branch (AGB) stars [18]. The CNO cycle is a stable process by which carbon, nitrogen and oxygen nuclei are used as catalysts in the conversion of hydrogen to helium. The typical reaction sequence is

$$^{12}\mathrm{C}(p,\gamma)\,^{13}\mathrm{N}(\beta)\,^{13}\mathrm{C}(p,\gamma)\,^{14}\mathrm{N}(p,\gamma)\,^{15}\mathrm{O}(\beta)\,^{15}\mathrm{N}(p,\gamma)\,(^{12}\mathrm{C}+\alpha).$$

In AGB stars of mass 1-3 $\mathrm{M}_{\odot}$ ($\mathrm{M}_{\odot} \equiv 1.989\cdot 10^{33}$ g, the mass of the Sun), significant neutron flux can be created in the helium burning region via the $^{13}\mathrm{C}(\alpha,n)$ reaction. This neutron flux can then give rise to neutron capture on CNO cycle nuclei and the reaction chain

$$^{12}\mathrm{C}(n,\gamma)\,^{13}\mathrm{C}(n,\gamma)\,^{14}\mathrm{C}(n,\gamma)\,^{15}\mathrm{C}(\beta)\,^{15}\mathrm{N}(n,\gamma)\,^{16}\mathrm{N}(\beta)\,^{16}\mathrm{O}(n,\gamma)\,^{17}\mathrm{O}(n,\alpha)\,^{14}\mathrm{C}.$$

The slowest of these reactions is $^{14}\mathrm{C}(n,\gamma)\,^{15}\mathrm{C}$ [19], and therefore a significant buildup of $^{14}\mathrm{C}$ may occur.

Finally, the r-process that might take place in core-collapse supernovae may be significantly influenced by the availability of light seed nuclei produced in a neutrino driven wind environment [20]. The rate at which the reactions take place to form seed nuclei will determine whether the neutron to seed ratio is high enough for heavy r-process nuclei to be formed. One of the reactions affecting the production of seed nuclei is (n,γ) on $^{14}\mathrm{C}$ which is formed in the sequence

$$^{4}\mathrm{He}(\alpha n,\gamma)\,^{9}\mathrm{Be}(\alpha,n)\,^{12}\mathrm{C}(n,\gamma)\,^{13}\mathrm{C}(n,\gamma)\,^{14}\mathrm{C}\ \text{or}$$
$$^{4}\mathrm{He}(\alpha n,\gamma)\,^{9}\mathrm{Be}(n,\gamma)\,^{10}\mathrm{Be}(\alpha,\gamma)\,^{14}\mathrm{C}.$$

Due to the high temperature of such an environment ($\sim 3\cdot 10^{9}$ K) higher energies for the (n,γ) cross section is needed for such a scenario, up to about 1 MeV [19].

The first direct measurement of $^{14}\mathrm{C}(n,\gamma)$ is described in Ref. [21]. In this measurement the Maxwellian averaged cross section (MAC) of 1.72±0.43 μb was obtained. The MAC is related to the energy dependent cross section, σ(E) by

$$MAC \equiv \left[\frac{\langle \sigma v \rangle}{v_T}\right]_{kT} = 1.5\sigma(E)\left[\frac{kT}{E}\right]^{1/2}. \qquad (1.5)$$

Thus this experiment yielded a σ(23.3 keV)=1.1±0.28 μb. Calculated values at the time were $\sigma(25\ \mathrm{keV}) = 5.1\ \mu\mathrm{b}$ [22] and $\sigma(25\ \mathrm{keV}) = 100\ \mu\mathrm{b}$ [23]. Even disregarding the calculation of [23] as being much too large in light of the measurement of [21], this still left a factor of ~5 discrepancy between the calculated and measured value. This measurement was eventually repeated [19] and a significantly larger value for the cross section was found because of an error

in Ref. [21] that arose from the activation of the container for the ^{14}C powder as the result of a previous experiment with that apparatus. By the time the measurement in Ref. [19] was made, sufficient time had elapsed to reduce the activity of the container to an acceptably low level. The resulting radiative neutron capture cross section found in [19] was $\sigma(23.3\ \text{keV}) = 5.2 \pm 0.3\ \mu\text{b}$.

Indirect methods have also been applied to this reaction, notably Coulomb breakup of ^{15}C [24], [25], [13], [26], [27] and charge symmetry for the ^{15}C-^{15}F mirror nuclei [10]. A summary of the values for the cross section at 23.3 keV is given in Table 1. In cases where the cross section was not explicitly given in the reference it was calculated based on the information given.

Table 1. Comparison of (n,γ) cross sections on ^{14}C.

Reference	type of measurement	σ(23.3 keV) (μb)
[26]	Breakup	2.6±0.9
[27]	Breakup	4.5±0.5
[10]	Mirror nucleus	5.3±0.3
[13]	Breakup, CDCC	4.48±0.09
[25]	Breakup	4.1±0.4
[19]	Direct	5.2±0.3

C. Objectives

The aim of this work is to investigate the feasibility of the method of determining the SF of [8]. As part of this, the ANC for $^{15}\text{C} \leftrightarrow {}^{14}\text{C}+\text{n}$ will be determined and will then be used to calculate the astrophysical radiative neutron capture on ^{14}C. This capture rate can then be compared with the most recent direct measurement [19].

D. Dissertation outline

This dissertation consists of five chapters, the first of which was meant to provide the background and motivation for this work, including a review of the current state of affairs with respect to the neutron capture cross section and a review of the relevant literature. The next chapter, Chapter II, will cover the theoretical basis of this work, expanding on many of the ideas presented in Chapter I. Chapter III covers the experimental setup and details, including the multipole-dipole-multipole (MDM) spectrometer used to make the HI transfer and forward kinematics (d,p) measurements and the newly commissioned Texas-Edinburgh-Catania Silicon Array (TECSA) used for the inverse (d,p) reaction. Next is Chapter IV, which covers the analysis of the data from the various measurements and the extraction of the ANCs, as well as the investigation of the new method to extract the SF. Finally, the results of the direct capture calculations are given in Chapter V, along with a conclusion.

CHAPTER II

THEORY

A. Reaction kinematics

A reaction of a particle *a* incident on a nucleus *A* resulting in the nuclei *b* and *B* can be expressed as

$$a + A \rightarrow b + B \text{ or } \mathrm{A}(\mathrm{a},\mathrm{b})\mathrm{B}. \tag{2.1}$$

The initial system of *a* and *A* is the entrance channel, which will be denoted as α, whereas the exit channel *b* + *B* will be denoted as β. The total kinetic energy of the entrance channel is

$$E_{tot} = \frac{1}{2} m_a \mathrm{v}_a^2 + \frac{1}{2} m_A \mathrm{v}_A^2, \tag{2.2}$$

where $\mathrm{v}_{a(A)}$ and $m_{a(A)}$ are the velocity and mass of *a*(*A*) respectively. These velocities are in a fixed laboratory system, but for many calculations it is more convenient to work in a system in which the center of mass is fixed. In any system the position of the center of mass is defined as

$$\vec{S} = (m_a \vec{r}_a + m_A \vec{r}_A) / m_{aA}, \tag{2.3}$$

where $m_{aA} = m_a + m_A$. Also the relative position of *a* and *A* can be expressed as a vector

$$\vec{R} = \vec{r}_a - \vec{r}_A. \tag{2.4}$$

Solving for $\vec{r}_a$ and $\vec{r}_A$ in terms of $\vec{S}$, $\vec{R}$, m_a, and m_A, the total energy can be rewritten as

$$E_{tot} = \frac{1}{2} m_{aA} \dot{S}^2 + \frac{1}{2} \mu_{aA} \dot{R}^2. \tag{2.5}$$

In the above equation $\mu_{aA} = \dfrac{m_a m_A}{m_{aA}}$ is the reduced mass of particles *a* and *A*. The first term is the energy of the motion of the center of mass and the second term is the energy of the relative motion of the two particles. If $\mathrm{v}_A = 0$ as is the case for a stationary target being bombarded by a particle beam, the energy in the CM system can be related to that of the lab system as

$$E_{CM} = \frac{m_A}{m_{aA}} E_a = \frac{1}{2} \mu_{aA} \mathrm{v}_a^2. \tag{2.6}$$

Since the measurements of the angular distributions of cross sections are made with a fixed target and measured in the laboratory frame, it is necessary to relate the measured lab angle to the angle in the CM frame of reference, which is used in the theories that describe the interactions. The laboratory velocity of a particle can be decomposed into a sum of the velocity of the center of mass and the CM velocity of that particle as

$$\vec{v} = \dot{\vec{S}} + \vec{v}_{CM}\,, \tag{2.7}$$

which is illustrated in Fig. 1.

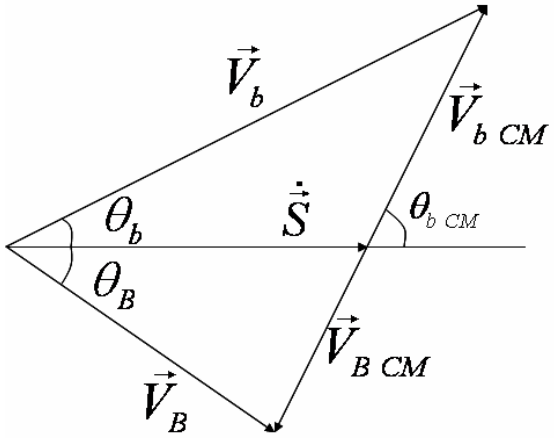

Fig. 1. Vector diagram showing the velocities and angles of the particles *B* and *b* in the exit channel of the reaction defined by (2.1) in the lab and CM frames.

From this one can relate the angles in the two frames by

$$\tan(\theta_{lab}) = \frac{\mathrm{v}_{CM}\sin(\theta_{CM})}{\dot{S} + \mathrm{v}_{CM}\cos(\theta_{CM})}. \tag{2.8}$$

The solid angles in the two frames are related by

$$\frac{d\sigma(\theta_{lab})}{d\Omega_{lab}} = \frac{(1+\rho^2+2\rho\cos\theta_{CM})^{\frac{3}{2}}}{|1+\rho\cos\theta_{CM}|}\frac{d\sigma(\theta_{CM})}{d\Omega_{CM}}\,, \tag{2.9}$$

where $\rho = \left[\frac{m_a m_b}{m_A m_B}\frac{E}{Q+E}\right]^{\frac{1}{2}}$.

B. Quantum description of scattering and reactions

The non-relativistic motion of the particle *a* of Eq. (2.1) in the entrance channel α is described by the Schrödinger equation:

$$(H-E)\Psi = 0\,, \tag{2.10}$$

where H is the total Hamiltonian, E is the total energy, and Ψ is the total wave function, which includes both the relative motion and the internal configuration of the particles. It can be decomposed into a part Φ that depends on the internal configuration only and a part ψ that depends only on the external coordinates. The Hamiltonian can be written as

$$H = H_a + H_A + T_\alpha + V_\alpha. \tag{2.11}$$

Here T_α and V_α are the kinetic energy operator and the potential energy, respectively, for the channel α. $H_{a(A)}$ is the Hamiltonian that describes the internal structure of *a*(*A*). The Schrödinger equation can be rewritten as

$$(E - H_\alpha - T_\alpha)\Psi_\alpha = V_\alpha \Psi_\alpha. \tag{2.12}$$

To find an equation that describes the motion in the exit channel, one can multiply (2.12) by the wave function describing the internal configuration of the exit channel and integrate over the internal coordinates. In the case of elastic scattering, this wave function is the same as for the entrance channel Φ_α. If a transition to a second channel (here denoted as β) occurs through inelastic scattering or a reaction, it is Φ_β and (2.12) becomes

$$(E_\beta - T_\beta)\psi_\beta = (\Phi_\beta, V_\beta \Psi_\alpha)\,, \tag{2.13}$$

where E_β is the kinetic energy of relative motion in the channel β, and using the convention that

$$(\Phi_\beta, V_\beta \Psi_\alpha) \equiv \int \Phi_\beta^* V_\beta \Psi_\alpha d(\text{internal coordinates}). \tag{2.14}$$

Equation (2.13) can be rewritten in terms of a Green's function which solves the equation

$$(E_\beta - T_\beta) G_\beta^0(\vec{r}_\beta - \vec{r}'_\beta) = \delta(\vec{r}_\beta - \vec{r}'_\beta). \tag{2.15}$$

By the definition of the delta function, the general solution to (2.13) in terms of (2.15) is

$$\psi_\beta = \int G_\beta^0(\vec{r}_\beta, \vec{r}'_\beta)(\Phi_\beta, V_\beta \Psi_\alpha) d\vec{r}'_\beta. \tag{2.16}$$

A solution to (2.15) is

$$G_\beta^{0(+)}(\vec{r}-\vec{r}') \underset{\text{at large r}}{=} -\left(\frac{2m_\beta}{4\pi\hbar^2}\right)\frac{\exp(ik_\beta r)}{r}\exp(-i\vec{k}'_\beta\cdot\vec{r}). \tag{2.17}$$

Inserting (2.17) into (2.16) yields the scattering amplitude

$$f_{\beta\alpha}(\theta) = -\frac{m_\beta}{2\pi\hbar}\int \exp(-i\vec{k}_\beta\cdot\vec{r})(\Phi_\beta, V_\beta\Psi_\alpha^{(+)})d\vec{r}. \tag{2.18}$$

Using the convention that $\langle f \mid g\rangle \equiv \int f^* g d(\text{all coordinates})$, (2.18) can be rewritten as a transition matrix element

$$\tilde{T}_{\beta\alpha} = \langle \phi_\beta \mid V_\beta \mid \Psi_\alpha^{(+)}\rangle, \tag{2.19}$$

where $\phi_\beta = \exp(-i\vec{k}_\beta\cdot\vec{r}_\beta)\Phi_\beta$ is the wave function describing the plane wave motion of a free particle.

In Eq. (2.19) the motion of the particles in the outgoing channel β is described by a plane wave, and the entrance channel still contains the exact solution of Eq. (2.10), which takes into account all processes and interactions that can occur. It is useful to introduce a potential U(r) that depends only on the relative coordinate and describes the motion in the channel. This potential could be chosen such that it describes well the elastic scattering in the given channel, for example. Separating this potential from the total V_β and defining an appropriate Green's function with it, after manipulations similar to those from (2.13) to (2.18), Eq. (2.19) becomes

$$\tilde{T}_{\beta\alpha} = \langle \chi_\beta^{(-)}\Phi_\beta \mid V_\beta - U_\beta \mid \Psi_\alpha^{(+)}\rangle . \tag{2.20}$$

Here χ_β is a distorted wave which describes the motion in the exit channel β on account of the potential U, the description of which is given in the next section.

C. Optical model potentials

It is not possible to calculate the complete, exact wave function Ψ_α. The reaction described by (2.19) is a complicated, many body problem involving a large number of possible reaction channels. At typical laboratory energies, nuclear interactions are dominated by elastic scattering and other open direct reaction channels can be treated as small perturbations. In these situations, an optical model potential (OMP) is a useful tool to describe the interaction. The OMP reduces the problem from a many body problem to that of a two body problem with a

potential that depends on the relative coordinate of the two particles in the channel. Because of the availability of other reaction channels, flux is not conserved and thus the OMP should be complex. Global potentials for nucleon-nucleus systems are available that consist of many fits to data at different energies and with different targets that are then interpolated to make a general potential for new reactions and energies. There are also OMP parameterizations available for some light particles such as deuterons and tritons. For a transfer reaction where elastic scattering will also take place (and typically at a cross section orders of magnitude higher than the transfer), the typical approach is to measure the elastic scattering angular distribution as well and to fit an OMP to that data which can then be used for the entrance channel for the transfer. The OMP for the exit channel for the transfer can then be determined by fitting to elastic scattering from another experiment or from the use of a global potential.

Typically the shape of the potential describing the nuclear interaction is that of a Woods-Saxon (WS), which is given by

$$V_{WS} = -\frac{V_0}{1+\exp\left(\frac{r-R_0}{a_0}\right)}. \tag{2.21}$$

This form is used for both the real and imaginary (absorptive) terms. R_0 is often parameterized as

$$R_0 = r_0(a^{\frac{1}{3}} + A^{\frac{1}{3}}) \tag{2.22}$$

where $r_0 \approx 1.2$ fm and a and A are the numbers of nucleons in the two nuclei. This works fairly well in most cases, however it should be noted that it is an approximation.

Similarly, a_0, the diffuseness, is often taken as ≈ 0.6 fm. The radius and diffuseness can be varied together to produce the same potential for different values, so it may be useful to fix one parameter at an arbitrary value and vary the other to fit the data. Sometimes a surface term is added to the imaginary term to account for collective surface modes, peripheral collisions resulting in transfers and other surface-peaked processes. This term takes the form

$$W_s = \frac{dW_{WS}}{dr} \tag{2.23}$$

where W_{WS} is the imaginary volume term and has the same form as (2.21).

For charged particles, the Coulomb potential must also be considered. For particles at a large distance this is simply that of two point charges, but a charged projectile near the target nucleus will experience a potential determined by the charge distribution of the two nuclei. For a uniform charge distribution, this can be written as

$$V_c = Z_a Z_A e^2 * \begin{cases} \left(\frac{3}{2} - \frac{r^2}{2R_c^2}\right)\frac{1}{R_c} & \text{for } r \le R_c \\ \frac{1}{r} & \text{for } r > R_c \end{cases} \tag{2.24}$$

A spin orbit (SO) term may be added to account for the coupling of the spin of the projectile to the relative orbital angular momentum of the channel.

The total OMP can be written as

$$U_{OMP} = V + i\left(W + W_S\right) + V_C + V_{SO.} \tag{2.25}$$

Equation (2.25) has up to 13 free parameters if independent geometries are used that must be found when fitting to scattering data. Often some of the geometries are chosen to be identical. Even if the SO term is neglected and the imaginary surface and volume geometries are set to be identical as is often done, this still leaves eight parameters.

One alternative approach to this problem is to use a so-called double folding procedure to obtain an OMP. Such a procedure is described in Ref. [28]. The first step in this method is to calculate the nuclear density distributions in a Hartree-Fock calculation. Once the densities are calculated a double integral over the two nuclei is performed to get the potential

$$V_{fold}(r) = \iint d\vec{r}_1 d\vec{r}_2 \rho_1(r_1)\rho(r_2) v_{eff}(\vec{r}_1 + \vec{r} - \vec{r}_2). \tag{2.26}$$

An appropriate nucleon-nucleon interaction potential (v_{eff}) must be chosen. In [28] the Jeukenne, Lejeune and Mahaux [29] (JLM) effective interaction was used, as well as several other interactions and the JLM was found to give the best results for the nuclei studied. To utilize the JLM effective interaction, which is energy and density dependent, Eq. (2.26) is rewritten as:

$$V(r) = \iint d\vec{r}_1 d\vec{r}_2 \rho_1(r_1)\rho_2(r_2) v_0(\rho, E)\delta(\vec{s}), \tag{2.27}$$

where $\vec{s} = \vec{r}_1 + \vec{r} - \vec{r}_2$ and

$$v_0(\rho, E) = \frac{V_0(\rho, E) + iW_0(\rho, E)}{\rho} \tag{2.28}$$

has independent real and imaginary parts starting from elastic scattering of nucleons in infinite nuclear matter of density ρ. The local density, ρ, is approximated as

$$\rho = \left[\rho_1\left(\vec{r}_1 + \frac{\vec{s}}{2}\right)\rho_2\left(\vec{r}_2 - \frac{\vec{s}}{2}\right)\right]^{1/2}. \tag{2.29}$$

An improvement in the local density approximation is achieved by replacing the delta function in (2.27) with a Gaussian form factor

$$g(\vec{s}) = \left(\frac{1}{t\sqrt{\pi}}\right)^3 \exp\left(\frac{-\vec{s}^2}{t^2}\right), \tag{2.30}$$

where *t* is a range parameter. The resulting double folding potential is

$$U(r) = N_V V_{fold}(r) + iN_W W_{fold}(r). \tag{2.31}$$

There are only two parameters in Eq. (2.31), or four if the ranges are left free, compared with six in an analogous potential of the WS form. Furthermore, since differences in the nuclei for the channel being described are accounted for in the density calculations, standard values of these parameters (N_v=0.37, N_w=1.00, t_v=1.20 fm and t_r=1.75 fm) turned out to work well for a variety of nuclei.

D. Spectroscopic factors and asymptotic normalization coefficients

The spectroscopic factor (SF) is a measure of the probability of finding, for example in the case of direct nucleon capture, the internal configuration of a core (*A*) plus a nucleon (*n*- either a proton or a neutron) in the composite residual nucleus ($B = A + n$). This is expressed formally in terms of the norm of the overlap function:

$$SF_{nlj} = N\int_0^\infty \left| I^B_{An(nlj)}(\vec{r})\right|^2 r^2 dr\,, \tag{2.32}$$

where the overlap function is defined as [9]

$$\begin{aligned} I^B_{An(nlj)} &= \left\langle \Phi_A(\zeta_A)\Phi_n(\zeta_n) \,|\, \Phi_B(\zeta_A,\zeta_n;\vec{r})\right\rangle \\ &= \sum_{l_B m_{l_B} j_B m_{j_B}} \left\langle J_A M_A j_B m_{j_B} \,\middle|\, J_B M_B\right\rangle \left\langle J_n M_n l_B m_{l_B} \,\middle|\, j_B m_{j_B}\right\rangle i^{l_B} Y_{l_B m_{l_B}}(\hat{r}_{An}) I^B_{An(l_B j_B)}(r_{An}). \end{aligned} \tag{2.33}$$

Here the overlap function, $I^B_{An(nlj)}(\vec{r})$, is proportional to the probability of removing a nucleon (either a proton or a neutron) at position $\vec{r}$ from the composite system B and leaving the core in

the state described by the wave function Φ_A. The orbital is specified by the quantum numbers nlj which are the principal quantum number, the orbital angular momentum and the total angular momentum respectively. Context should make it clear whether *n* refers to a nucleon or a principal quantum number. ζ are the internal coordinates of the nucleus whereas $\vec{r}$ describes the motion of its center of mass. *N* is the antisymmetrization factor.

Far away from the nuclear interior, the tail of the radial overlap function is proportional to a Whittaker function over the radius, r, as

$$I^B_{An(nlj)}(r) \overset{r>R}{\approx} C^B_{An(nlj)} \frac{W_{\eta_B, l_B+\frac{1}{2}}(2\kappa_B r)}{r}, \tag{2.34}$$

which, in the case of *n* being a neutron with the Sommerfeld parameter $\eta = 0$, reduces to

$$I^B_{An(nlj)}(r) \overset{r>R}{\approx} C^B_{An(nlj)}(i\kappa) h_l(i\kappa r) \tag{2.35}$$

where $C^B_{An(lj)}$ is the asymptotic normalization coefficient (ANC) and defines the amplitude, $\kappa = \sqrt{2\mu_{An}\varepsilon_{An}}$ is the wave number with μ_{An} as the reduced mass and ε_{An} as the nucleon separation energy, and h_l is a Hankel function.

Some reactions, such as direct proton capture below the Coulomb barrier, are very peripheral and their cross sections can be accurately calculated if the ANC is known. This is very useful since such sub-Coulomb capture reactions are extremely difficult to directly measure in a terrestrial laboratory. Not only is the cross section extremely low, which results in a very low count rate that requires long run times and makes one very sensitive to background, Coulomb screening may significantly affect results. In contrast, the ANC can be extracted from a heavy-ion (HI) transfer reaction at a laboratory energy selected to make the reaction peripheral in order to keep the approximation in (2.34) valid. Such a HI transfer reaction has a cross section orders of magnitude higher than that of the direct capture reaction, yet the information gained (the ANC) is directly applicable.

From (2.34) it is apparent that the radial overlap function dies off exponentially at large r, and therefore the largest contribution to the SF will be from the nuclear interior. Thus, while a peripheral HI transfer reaction described above would be appropriate for gaining information about the tail of the overlap function, it will not probe the nuclear interior and will not be useful in experimentally measuring the SF. At higher energies transfer reactions (both HI and (*d*,*p*))

become less peripheral and begin to give information about the nuclear interior. However, for these non-peripheral reactions the traditional method of extracting the SF by normalizing the distorted wave Born approximation (DWBA) cross section (see below) to the experimentally measured cross section is inadequate due to antisymmetrization and many-body effects making the single particle approximation used invalid.

The cross section for a transfer reaction $\alpha = A + a \rightarrow B + b = \beta$, where a particle *x* is transferred from *a* to *A*, may be expressed, omitting the notation for spin and angular momentum, in terms of the transfer matrix element

$$\left(\frac{d\sigma}{d\Omega}\right)_{\beta\alpha} = \frac{\mu_\alpha \mu_\beta}{\left(2\pi\hbar^2\right)^2}\frac{k_\beta}{k_\alpha}\left|\tilde{T}_{\beta\alpha}\right|^2,$$

where $\mu_{\alpha(\beta)}$ and $k_{\alpha(\beta)}$ are the reduced mass and the wave number respectively in channel $\alpha(\beta)$ and the transfer matrix element

$$\tilde{T}_{\beta\alpha} = \left\langle \chi_\beta^{(-)}\Phi_\beta \left| V_\beta - U_\beta \right| \Psi_\alpha^{(+)} \right\rangle. \tag{2.36}$$

Here $\Psi_\alpha^{(+)}$ is an exact solution to the Schrödinger equation and includes both energy of the relative motion and the internal structure of the entrance channel α. $V_\beta - U_\beta$ is the interaction potential in post form. $\chi_\beta^{(-)}$ is the wave function of the relative motion in the exit channel *β* and $\Phi_\beta = \Phi_b \Phi_B$ is the bound state wave function for the intrinsic state of the nuclei *b* and *B* in the exit channel. This transfer matrix element contains the amplitude of the transition from entrance channel *α* to the exit channel *β*. Because $\Psi_\alpha^{(+)}$ is an exact solution of the Schrödinger equation it can be decomposed into a sum over all physically allowable eigenfunctions making the transition amplitude

$$\tilde{T}_{\beta\alpha} = \sum_\gamma \left\langle \chi_\beta^{(-)}\Phi_\beta \left| V_\beta - U_\beta \right| \Phi_\gamma \psi_\gamma^{(+)} \right\rangle, \tag{2.37}$$

where $\sum_\gamma |\,\Phi_\gamma)(\Phi_\gamma\,| = 1$. This shows that all available channels (γ) may contribute to the transition probability α→β.

It is not possible to calculate the exact solution, Ψ_α, to the many-body scattering problem. However, this solution can be approximated to first order as the product of a wave

function describing the internal configuration of the nuclei in channel α and a wave function describing the relative motion in that channel,

$$\Psi_{\alpha}^{(+)} \approx \Phi_{\alpha}\chi_{\alpha}^{(+)}. \tag{2.38}$$

Inserting this approximation into the transition matrix (2.36) above gives

$$\tilde{T}_{\beta\alpha}^{DWBA} = \left\langle \chi_{\beta}^{(-)}\Phi_{\beta}\left|V_{\beta} - U_{\beta}\right|\Phi_{\alpha}\chi_{\alpha}^{(+)}\right\rangle, \tag{2.39}$$

the DWBA transition matrix, which essentially assumes a one-step process.

The distorted waves that describe the relative motion in the entrance and exit channels are solutions to the Schrödinger equation where the potential U is a complex optical model potential, typically in the form of a Wood-Saxon potential that has been fitted to elastic scattering data. Such a fit to elastic scattering data ensures the correct form for the distorted waves asymptotically as r→∞, but may not be accurate near the nuclear surface where the reaction typically takes place.

Another approximation taking place is that in the DWBA only the direct reaction from entrance channel α to the exit channel β is considered. The other contributions to the matrix element shown explicitly in (2.37) are neglected, which for a direct reaction is usually a good approximation. For less peripheral reactions at higher energies, where compound nucleus formation or multi-step processes may take place, this approximation becomes less appropriate.

Equation (2.39) may be written to show explicitly the bound state wave functions for the nuclei in the channels α and β:

$$\tilde{T}_{\beta\alpha}^{DWBA} = \left\langle \chi_{\beta}^{(-)}\Phi_{B}\Phi_{b}\left|V_{\beta} - U_{\beta}\right|\Phi_{A}\Phi_{a}\chi_{\alpha}^{(+)}\right\rangle.$$

With some rearranging and utilization of the definition of the overlap function (2.33) the transfer matrix becomes

$$\tilde{T}_{\beta\alpha}^{DWBA} = \left\langle \chi_{\beta}^{(-)}I_{B}^{A}(\vec{r})\left|V_{\beta} - U_{\beta}\right|I_{b}^{a}(\vec{r})\chi_{\alpha}^{(+)}\right\rangle. \tag{2.40}$$

In the single particle approximation the radial overlap function may be written [6] as

$$I_{Al_Bj_B}^{B}(r) \approx I_{Al_Bj_B}^{B(sp)}(r) = [SF^{(sp)}]^{1/2}\phi_{n_Bl_Bj_B}(r), \tag{2.41}$$

where $\varphi_{n_Bl_Bj_B}(r)$ is the normalized single particle radial wave function. Subscripts denoting the principal quantum number *n*, the orbital angular momentum *l* and the total angular momentum *j* have been added for clarity. Using this single-particle approximation and bringing out of the

integration the SFs, the DWBA cross section can be parameterized in terms of the single particle SFs as

$$\frac{d\sigma}{d\Omega} = \sum_{j_B l_B} SF^{(sp)}_{Axl_B j_B} SF^{(sp)}_{bxl_B j_B} \sigma^{DWBA}_{l_B j_B l_a j_a}(\theta). \tag{2.42}$$

Typically (2.42) is used to determine SFs from normalization to experimental data in order to compare with SFs from shell model calculations. It is important to note, however, that the SFs in (2.42) are, because of the approximation in (2.41), actually single particle SFs and are not necessarily directly comparable with the SF from (2.32), which is dependent on the behavior of the radial overlap function in the nuclear interior. If the reaction used to get the single-particle SF is peripheral, the nuclear interior is not probed and therefore the result is extremely model-dependent. On the other hand, a non-peripheral reaction will likely not be accurately described by the single-particle approximation as many body effects become important and other channels contribute to the cross section.

It has been shown [6] that if the reaction is peripheral the more appropriate quantity to extract is the ANC. In the asymptotic region the radial bound state wave function of (2.41) may be written as

$$\varphi_{n_B l_B j_B}(r) \xrightarrow{r>R_N} b_{l_B j_B} \frac{W_{-\eta_B, l_B+1/2}(2\kappa_B r)}{r} \tag{2.43}$$

for protons. A similar expression may be written for neutrons in terms of a Hankel function as (2.34) becomes (2.35) since $\eta = 0$. However, in the interior of the nucleus the shape of φ will depend on the geometry of the binding potential that is used to calculate it. This geometry is not typically known and this results in b_{lj} that depend on the geometry, specifically on the radius (r) and diffuseness (a) if the binding potential used is of the WS form.

Comparing (2.34), (2.41) and (2.43) gives the relationship between the ANC, the single-particle SF and the single-particle ANC ($b_{l_B j_B}$):

$$SF^{(sp)}_{l_B j_B} = \frac{(C^B_{Axl_B j_B})^2}{(b_{l_B j_B})^2}. \tag{2.44}$$

And from (2.44) the cross section may be parameterized in terms of the ANCs:

$$\frac{d\sigma}{d\Omega} = \sum_{j_B l_B} (C^B_{Axl_B j_B})^2 (C^a_{bxl_a j_a})^2 \frac{\sigma^{DW}_{l_B j_B l_a j_a}}{b^2_{Axl_B j_B} b^2_{bxl_a j_a}}. \tag{2.45}$$

The ratio of the calculated DWBA cross section to the product of the squared SPANCs is parameter-independent for a highly peripheral reaction, and thus, unlike the single-particle SF, the ANC extracted from a peripheral reaction is a parameter-independent quantity. Therefore, in (2.45), the ANC $C^{B}_{Axl_B j_B}$ can be determined in the above transfer reaction if one has prior knowledge of $C^{a}_{bxl_a j_a}$ from another measurement without detailed knowledge of the bound state wave functions and optical model potentials used in the analysis of that previous measurement. This is in contrast to the single particle SF which does require such information and is very model dependent. However, for non-peripheral processes such as s-wave neutron capture, the SF is clearly the more appropriate quantity, as the ANC only contains information about the normalization of the tail of the overlap function, and does not tell anything about the form of the overlap function in the interior. To solve this problem a reliable and model independent method to extract spectroscopic information for reactions with a non-trivial interior contribution is needed.

E. New method for extracting spectroscopic factors

A new method for extracting SFs has been proposed [8] that utilizes the ANC. It requires two measurements, one peripheral to determine the ANC and a second that has a significant contribution from the nuclear interior. In this second, non-peripheral experiment, the ANC is used to fix the external component of the reaction amplitude leaving the internal part whose normalization is determined by the SF. Given that most transfer reactions used to determine SFs in the laboratory are largely peripheral and that the overlap functions (and thus, via (2.32), the SFs) are dominated in their normalization by the interior region, fixing this significant external contribution is very important. The advantage to this approach is that it experimentally constrains variables that would otherwise be arbitrarily assigned, thus eliminating significant uncertainty in the final result.

To illustrate this, consider a (*d*,*p*) stripping reaction *A*(*d*,*p*)*B*. Equation (2.39) then becomes

$$\tilde{T}^{DWBA}_{\beta\alpha} = \left\langle \chi^{(-)}_{\beta} I^{B}_{An}(r) \middle| \Delta V \middle| \Phi_{pn} \chi^{(+)}_{\alpha} \right\rangle, \tag{2.46}$$

where Φ_{pn} is the bound-state deuteron wave function and ΔV is the interaction potential, which in post form is $V_{pn}+V_{pA}-U_{pB}$. The model independent definition of the SF is given by (2.32), however the antisymmeterization factor N will be absorbed into the overlap function in the following. Because the particle being transferred is a neutron, the Sommerfeld parameter η is zero, here again the Whittaker function in (2.34) reduces to a Hankel function (2.35):

$$I^{B}_{An(nlj)}(r) \overset{r>R}{\approx} C_{nlj} i\kappa h_{l}(i\kappa r)\,. \tag{2.47}$$

Furthermore, the overlap function may be assumed to be proportional to the bound-state wave function [8],

$$I^{B}_{An(nlj)}(r) = K_{nlj}\Phi_{An(nlj)}(r)\,. \tag{2.48}$$

Here K_{nlj} is an asymptotic proportionality constant that is related to the SPANC by

$$C_{lj} = K_{nlj} b_{nlj}\,. \tag{2.49}$$

Applying (2.48) and (2.49) to (2.47) gives the asymptotic behavior of the neutron single-particle wave function:

$$\Phi_{An(nlj)} \overset{r>R}{\approx} b_{nlj} i\kappa h_{l}(i\kappa r). \tag{2.50}$$

Given (2.32) and the assumed normalization of the bound-state wave function $\Phi_{An(nlj)}(r)$, it follows that $SF_{lj} = K^{2}_{nlj}$. However, it is important to remember that in the nuclear interior (2.48) may not hold as the overlap function becomes non-trivial and its behavior is not necessarily described by the single-particle bound-state wave function. Applying (2.48) to the transition amplitude (2.46) gives

$$\tilde{T}^{DWBA}_{\beta\alpha} = K_{nlj}\left\langle \chi^{(-)}_{\beta}\Phi_{An(nlj)}(r)\middle|\Delta V\middle|\Phi_{pn}\chi^{(+)}_{\alpha}\right\rangle. \tag{2.51}$$

This reaction amplitude can be split up into an exterior and an interior part as

$$\tilde{T}^{DWBA}_{\alpha\beta} = K_{nlj}\tilde{T}_{\mathrm{int}}[b] + K_{nlj} b_{nlj}\tilde{T}_{ext}\,. \tag{2.52}$$

In (2.52), due to the application of (2.50), the exterior matrix element, $\tilde{T}_{ext}$, does not depend on the SPANC. However, the interior component does depend on it through $\Phi_{An(nlj)}(r)$. From (2.49), the normalization of the exterior component is given by the ANC. This leaves the interior part whose normalization is through the SF.

To make use of (2.52) a transfer reaction must be selected that has a non-trivial contribution from the interior but that can still be described by DWBA. In order to compare such an experiment with the DW calculation, dividing (2.52) by the ANC and then taking the square norm gives a function

$$R^{DW}(b_{nlj}) = \left| \frac{\tilde{T}_{\text{int}}}{b_{nlj}} + \tilde{T}_{ext} \right|^2 , \tag{2.53}$$

whose experimentally measurable counterpart is

$$R^{\text{exp}} = \frac{\frac{d\sigma}{d\Omega}^{\text{exp}}}{C_{lj}^2} . \tag{2.54}$$

By setting (2.53) equal to (2.54), the SPANC, b_{nlj}, is experimentally fixed and the SF is given by

$$SF_{lj} = \frac{C_{lj}^2}{b_{nlj}^2} .$$

To reiterate, this approach requires two measurements. One experiment is needed to find the ANC if it is not already known. This could be, for instance, a HI transfer reaction that is performed at an energy selected to ensure that the reaction is peripheral (and thus that $\widetilde{T}_{\text{int}} = 0$). Once the ANC is known, a second reaction is measured that has a non-negligible $\widetilde{T}_{\text{int}}$. As the reaction becomes less peripheral, the dependence on b_{nlj} in (2.53) becomes stronger and thus the uncertainty of the SF is reduced, however at some point the assumptions inherent in DWBA analysis become less valid and thus the theory does not accurately describe the reaction taking place.

CHAPTER III

EXPERIMENTAL SETUP AND PROCEDURES

All experiments were performed at the Texas A&M University Cyclotron Institute with beams from the K500 superconducting cyclotron. The two experiments performed on the multipole-dipole-multipole (MDM) spectrometer were done using the beam analysis system (BAS). The beams impinged with thin foil targets in the reaction chamber of the MDM beamline and reaction products were measured using the high-resolution MDM spectrometer coupled with the Oxford ionization chamber detector. A third experiment was performed using the Momentum Acromat Recoil Spectrometer (MARS) and the Texas A&M-Edinburgh-Catania Silicon Array (TECSA).

In this chapter the following conventions will be used: the *z* axis is defined as the axis along which the beam travels, the *x* axis is the horizontal axis perpendicular to the path of the beam, and the *y* axis is the vertical axis perpendicular to the beam path. The angles θ and φ are used to represent angles in the *x*-*z* plane and in the *y*-*z* plane, respectively.

A. Beam analysis system

The Beam Analysis System [30] was constructed to improve the quality of beams available to the MDM spectrometer. It consists of seven dipoles and eight quadrupoles and has slits at three positions. Following entrance slits, the first four dipoles make an 88° counter-clockwise bend after which there is a second set of slits. Another set of three dipoles, which makes an 87° clock-wise bend, and a third set of slits serve to remove slit-scattered particles from the beam. The net result is a clean beam with a ΔE/E resolution of 1/2500 and about a 2 mm x 2 mm spot size on target. This resolution can be compared with a 1/700 resolution when using a K500 beam without the BAS [30]. The BAS was used for both of the MDM experiments described here. A simplified diagram of the beam line setup showing the K500, the BAS and the MDM beam line is shown in Fig. 2.

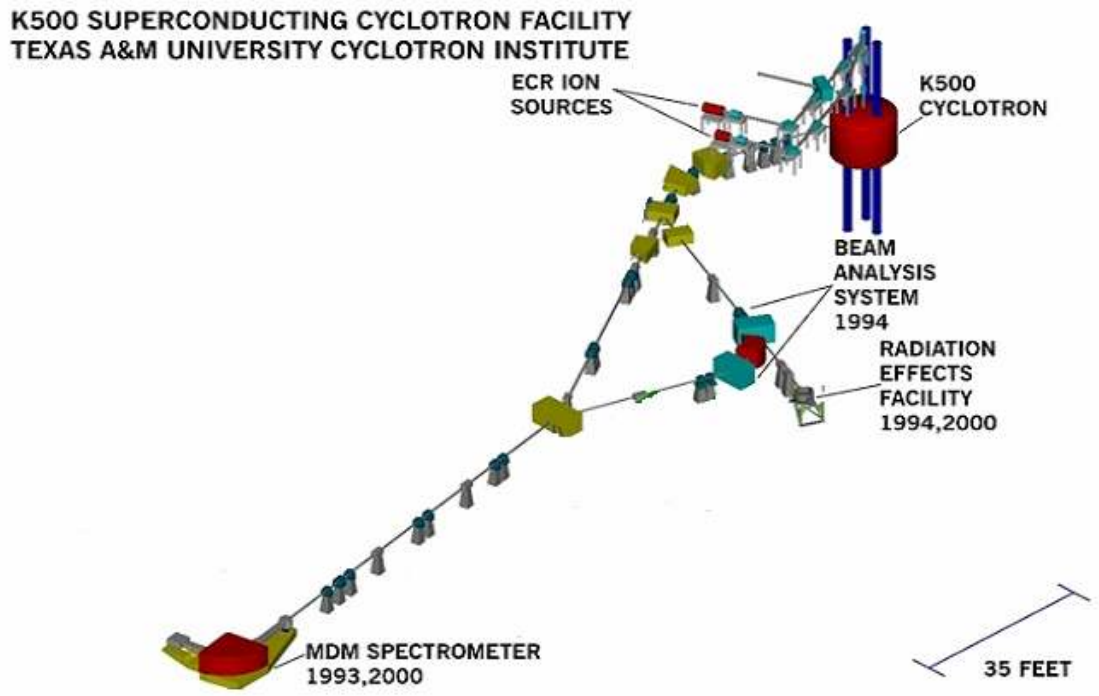

Fig. 2. Diagram of the beam line used in the experiments on MDM including the BAS.

B. MDM spectrometer

The MDM spectrometer [31] is a 1.6 m radius, 100° dipole spectrometer with an entrance quadrupole. At Texas A&M the coil was modified and some iron was added in the return yoke to increase the K-factor. The spectrometer is mounted on a rotatable arm that can be moved to measure a large range of scattering angles. The beam is focused on the target at the center of a sliding-seal reaction chamber. Downstream of this target position is a slit box with several collimators which define the angular acceptance of the spectrometer. For the measurement of the angular distribution of reaction cross sections a collimator with 4° acceptance in θ and 1° in φ was used, while a five finger collimator mask was used for position calibrations and to check the reconstruction of the target angle. A third collimator with a single centered slit with acceptance 0.1° in θ and 1° in φ was also used.

The dipole magnet is capable of fields in excess of 1 T. Entrance and exit field boundaries are designed to optimize the spectrometer performance. The exit boundary has a

concave radius of 0.5 m and serves to make the focal plane of the detector linear and perpendicular to the z axis. The 0.63 m convex radius of the entrance boundary corrects some aberrations that result from the curvature of the exit boundary. The entrance quadrupole magnet focuses the scattered particles in the y direction, reducing the necessary vertical gap for the dipole for a given acceptance in φ. The spectrometer is shown in Fig. 3.

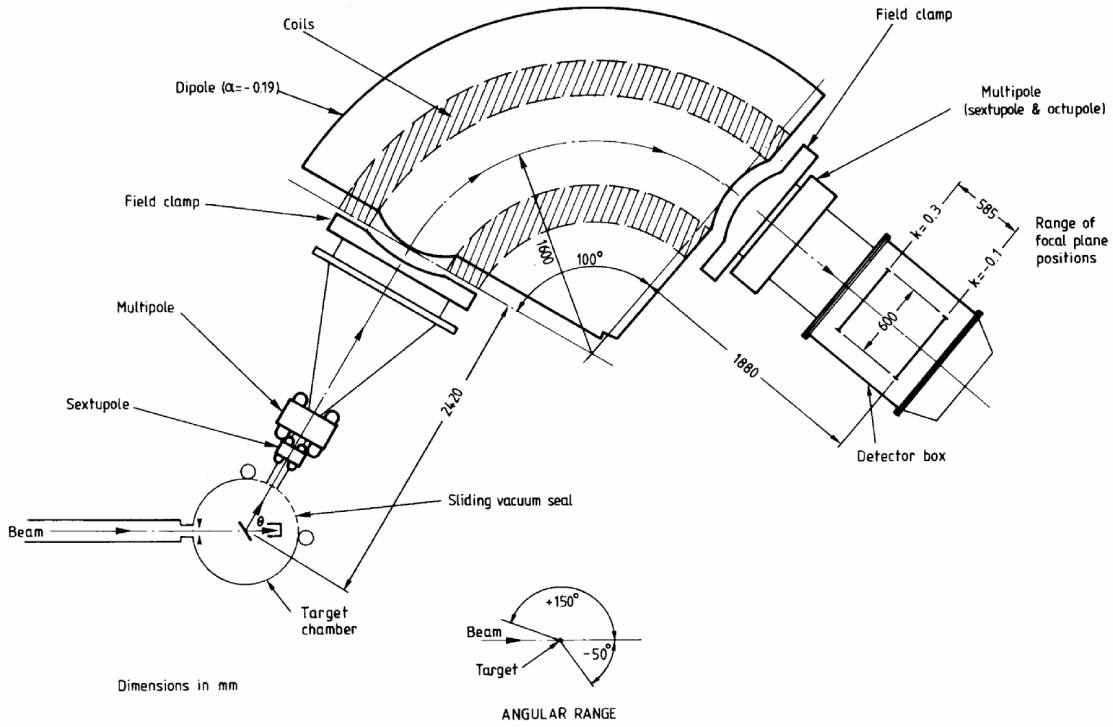

Figure 3. The MDM spectrometer. (D.M. Pringle *et al.* NIM A245 (1986) pg. 230-247)

C. Oxford detector

The Oxford detector is an ionization chamber detector placed after the exit of the MDM spectrometer and is used to measure the energy and trajectory of scattered particles (Fig. 4). The position of the detector along the z axis can be changed to place the focal plane inside of the detector. Entrance and exit windows are Aramica and are 25 and 50 μm thick, respectively. The inside of the detector is filled with isobutane gas at a pressure of about 50 torr. This gas is

continuously flowed in order to remove molecules broken down by the beam and to prevent charge build up.

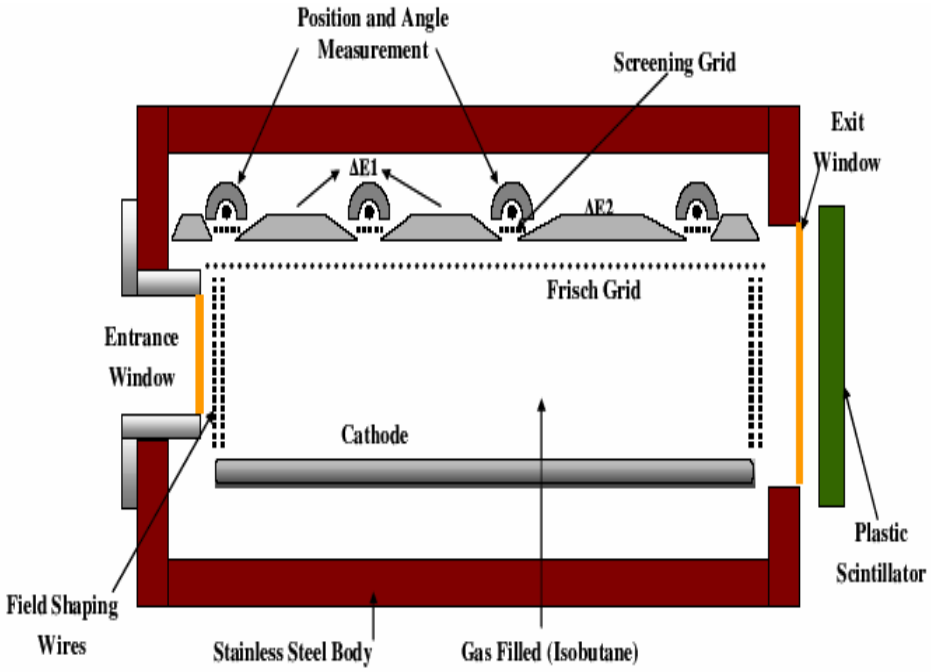

Fig. 4. The Oxford detector.

Energy loss is measured by means of anode plates along the top of the detector that collect electrons released by the ionization of gas molecules along the trajectory of the particles. These electrons are driven to the anode plates by the potential gradient between the negatively biased cathode (typically at -500 V) and the Frisch grid at the top of the detector just under the anode plates which are grounded through a resistor. Uniformity of the field in this region is achieved by biased rods running along the sides of the detector parallel to the *z* axis which are coupled between the two sides of the detector by field shaping wires connected to rods at the same potential on either side of the detector. The three anode plates along the top are split into two banks (the first and second make up ΔE1 and the third is ΔE2), giving two signals for energy loss along the particles' path in the detector. Due do noise in the second bank, only the first was used for particle identification.

The trajectory of particles in the detector is measured with four position-sensitive avalanche counters (ACs) that lie perpendicular to the *z* axis and slightly above the plane of the Frisch grid. These consist of very thin wires at high potential (about 1.5 kV) inside a half shell

that is kept at +100V. The bottom (towards the detector) has screening wires to contain the field. When electrons pass by the screening grid and experience the large field, an avalanche event occurs and the resulting charge is collected at both ends of the thin resistive central wire. Current readout at both ends is recorded and compared to find the position of the avalanche event. The difference in position at the first and fourth ACs was used to find the angle of the particle's trajectory inside of the detector (θ_d). This angle is compared with angles measured between the other sets of wires to check for consistency. The position in x in the focal plane is then found using θ_d and the position in x at the nearest AC. The position of the focal plane along z is known prior to the measurement by means of a RAYTRACE [32] calculation. The code RAYTRACE calculates the transformation of a vector representing the position, mass, charge and velocity of a particle through the optical matrices that represent the components of the system being calculated. It is very important in such a calculation that the field strengths and geometries be carefully determined for all of the elements entered, which has been done for the MDM spectrometer. The version of RAYTRACE used in this work has been set to accept several target angles and to give as output the positions and angles at a user-determined point along the z-axis after the spectrometer, taking into account the kinematic variation with angle. This output can then be checked against the observed scattering through the 5-finger mask.

After passing through the exit window, the particles traverse a 1.25" vacuum gap before being stopped in a BC-400 plastic scintillator. Photons resulting from the interaction of the particles with the scintillator are collected in two Hamamatsu 1960 photomultiplier tubes (PMTs), one on each side of the scintillator, which are in physical contact with the light guides No grease or optical epoxy was used between the light guides and the PMTs. Epoxy for this joint is not acceptable as different scintillators must be used with the same PMTs. Optical grease was not used in order to eliminate the possibility of a degradation of the light transmission due to imperfect application of the grease or movement of the scintillator or PMTs after application, such as during the pumping out of the chamber. The thickness of scintillator was chosen based on the energy and Z of the particles to be measured: a 0.25" scintillator backed by a 0.75" Lucite sheet was used for heavy ions and a 1.5" scintillator was used for (d,p) reactions. The use of two phototubes gives an energy signal that is largely independent of the x position of the particle in the scintillator.

D. Signal processing and data recording

For these measurements an updated electronic scheme was used to record the signals from the Oxford detector. In this new setup, all electronics were put close to the detector in the cave in an effort to eliminate the cable patches between the cave and the counting room as a source of noise. Canberra model 2004 charge-sensitive preamplifiers are connected via short 50 Ω coaxial cables to the ACs and the anode plates. These signals are then brought to a CAEN N568B 16ch shaper amplifier. The amplifier output is digitized by a Mesytec 32ch VME ADC. The PM anode one signals are digitized by a CAEN VME QDC while the anode two signals are used to make the trigger. A coincidence requirement between the two PMs is imposed using a Phillips 754 logic unit. The DAQ busy signal is used as a veto for the trigger to prevent triggers while data is being recorded.

The VME crate was controlled by a CES CBD 8210 and an SBS interface module connected via fiberoptic cable to a computer running a ROOT-based data transport program. Data was viewed online using a ROOT program and also recorded to disk for later offline analysis.

E. Particle Identification

Two methods of particle identification were used. In the case of heavy ions (HI), a plot of energy loss collected in the first anode in the ionization chamber (ΔE) versus the energy deposited when the particle stops in the plastic scintillator (E_{res}) was used in a standard ΔE- E_{res} scheme. Fig. 5 shows an example of such a particle identification with the particles of interest labled.

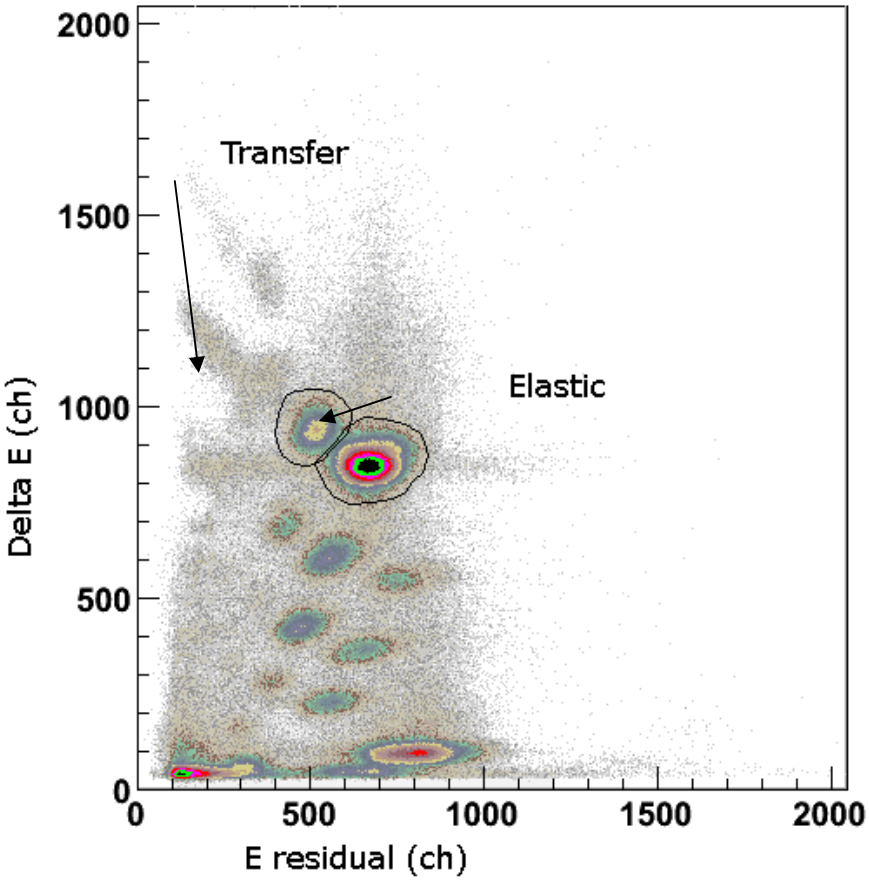

Fig. 5. Particle identification for the HI measurement.

The (*d*,*p*) reaction at E_d= 60 MeV required a different technique for particle identification due to the very small energy loss of both the deuterons and protons in the gas in the detector. For this reaction identification was done using only the scintillator. This could not be done using the same 0.25 " thick scintillator used in the HI experiment. Thus, in order to improve the separation of the protons and the deuterons, I designed a new 1.5" thick scintillator and light guides. This scintillator is sufficiently thick to stop the protons from the (*d*,*p*) reaction. While the total energy deposited by the protons and the inelastically scattered deuterons that also make it into the detector is similar, they have very different path lengths (about 28 mm for the protons and 4.7 mm for the inelastic deuterons) to which the light output of the scintillator is roughly proportional, and the signals allowed easy *p-d* separation (Fig 6).

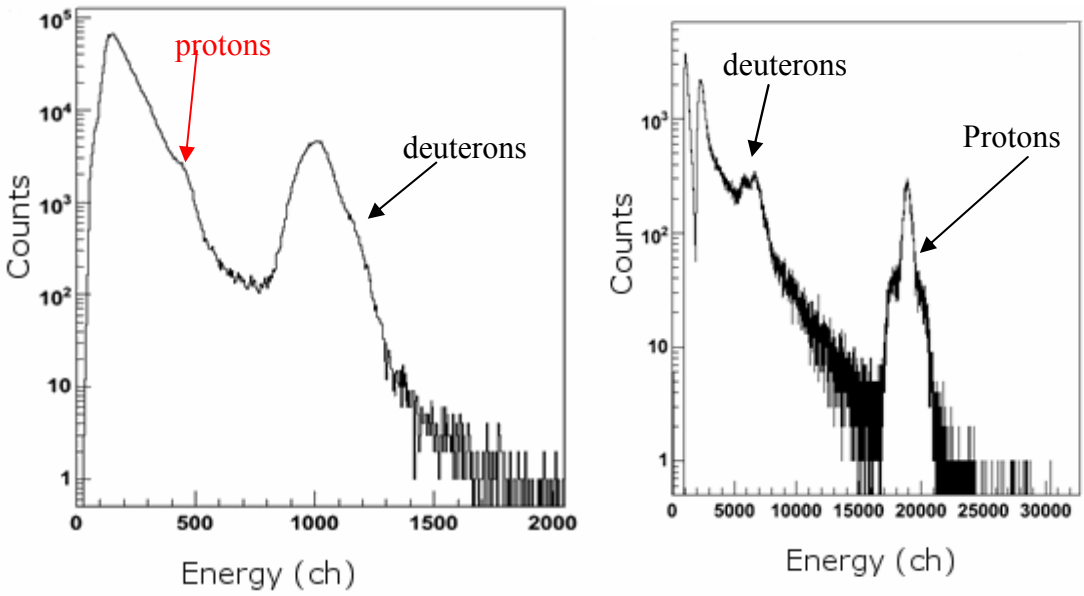

Fig. 6. Particle identification for $^{14}C(d,p)^{15}C$. On the left is particle identification with a 0.25" scintillator through which the particles punch through and on the right is the new 1.5" thick scintillator which stops even the high energy protons.

F. Position calibration of the Oxford detector

A position calibration is required to meaningfully compare the signals from the ACs. This is achieved by comparing the scattering of the beam on a thin gold target to a calculation by the code RAYTRACE. The input parameters for the MDM in RAYTRACE are well known. To get discrete positions at the ACs a five finger mask is used in the collimator position that consists of five slits 1° high in φ, 0.1° wide in θ and at a 0.765° spacing in θ with the middle slit at the central angle of the spectrometer. These five fingers are seen at each of the four ACs. A gate is placed on θ_d (determined by comparing the positions in the first and fourth ACs) for each finger, and the position of particles in these gates at each AC is plotted. RAYTRACE is used to calculate the trajectory of particles that passed through each slit through the spectrometer and gives the position of these particles at the entrance of the detector and their angle in the detector. For each wire a second-order polynomial is found that gives the calculated position in mm as a function of observed channel number.

G. Angle reconstruction

By the design of the spectrometer, in the focal plane the kinematic variation $k(\theta_t) \equiv \left(\frac{1}{p}\right)\frac{dp}{d\theta}$ cancels out the dependence on the scattering angle at the target so that the position in the focal plane (which is perpendicular to the *z*-axis by the design of the spectrometer) is only dependent on the magnetic rigidity of the particle (Bρ). Thus one can uniquely determine the scattering angle at the target, θ_t, for a given focal plane position by measuring the angle in the detector, θ_d.

To make use of this, a RAYTRACE calculation is performed for a given reaction or scattering process for several values of θ_t and for each value θ_d is found. From this calculation θ_t is plotted as a function of θ_d:

$$\theta_t = A + B\theta_d + C\theta_d^2 .$$

This calculation is then repeated at several energies so that the coefficients A,B and C can be plotted as second order polynomial functions of the focal plane position. It should be emphasized that this target angle reconstruction is accomplished with only RAYTRACE calculations, unlike the position calibration. However, it can be checked during the experiment by verifying that the reconstruction correctly reproduces the angles of the rays from the five finger mask and adjusted if necessary.

H. TECSA

The Texas-Edinburgh-Catania Silicon Detector Array, TECSA, is a high-efficiency array of annular sector silicon strip detectors designed to study reactions involving radioactive beams produced by MARS or by the facility upgrade at the Texas A&M Cyclotron [33]. The array consists of up to 16 Micron Semiconductor YY1-300 detectors with 8 detectors being used to measure position and energy loss and the other 8 behind in close geometry to measure the residual energy. Each detector has 16 annular ring sectors and is about 300 um thick. It is a cooperative effort of Texas A&M, the University of Edinburgh and the INFN Catania of the last two years. The electronics were from Edinburgh from the LEDA project and Catania provided the detectors and the deuterated polyethylene targets for the $d(^{14}C,p)^{15}C$ measurement. Texas

A&M provided the infrastructure and as part of that I designed the chambers for the detectors and targets as well as the target assembly and electrical feed through flanges.

The targets are on a holder with a rotating, six position wheel to allow for up to five targets and one target detector. The target detector is a dual-axis dual-lateral position sensitive detector from Micron [34], which allows for good position and energy resolution whilst minimizing the number of signals that must be processed. This target detector is in addition to the usual MARS target detector, upstream of TECSA, on which initial beam identification and tuning is performed and allows precise focusing of the secondary (radioactive) beam so as to minimize the beam spot size at the target and the associated degradation of the angular resolution. The target holder is on a precision linear motion track mounted to a plate in the detector chamber to allow reproducible control of the *z*-axis position of the target relative to the detector-as well as fixing the *x* and *y* position-and thus the angular range of the array. A schematic showing the general setup is given in Fig. 7. Fig. 8 shows the array mounted in its chamber on the back end of MARS.

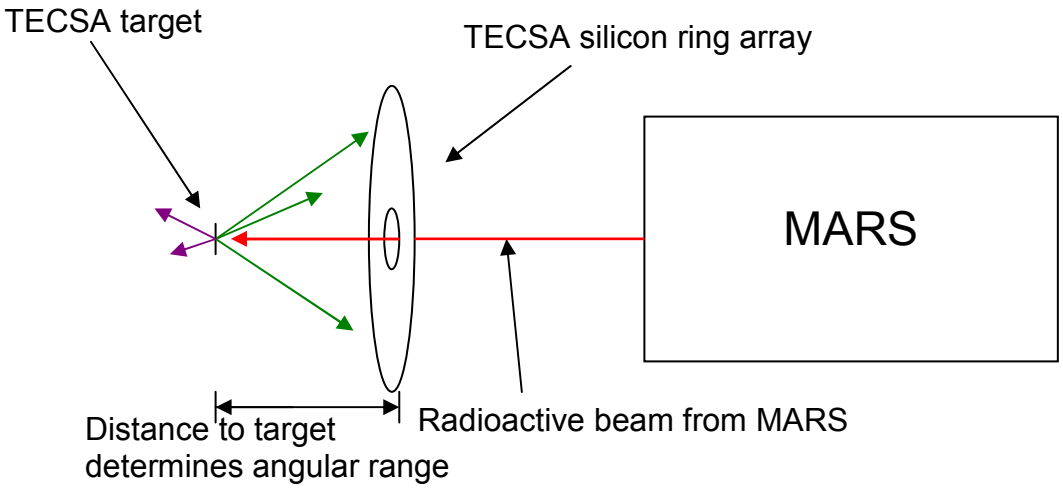

Fig. 7. A schematic showing the general setup of TECSA. Here the array is shown configured to measure backwards (lab) scattering, but it can be reconfigured to measure in the forward direction.

The electronic readout consists of RAL-108 16 channel preamplifiers (one for each YY1-300 detector) whose output goes into RAL-109 shaper-amplifiers [35]. The RAL shaper-amplifiers have both an analog output which is converted by Mesytec VME ADCs and an ECL

timing signal output. The ECL output is split between CAEN VME TDCs and an OR module which gives a NIM logic signal for an event in any of the detector strips. This OR signal is sent to a Phillips 756 logic unit where an OR condition is made for all of the strips in all of the detectors. This final OR is used in the master trigger and for the ADC gates. The ADC, TDC and scaler outputs are read using our in-house data acquisition system.

The commissioning run for TECSA was the $d(^{14}\mathrm{C},p)^{15}\mathrm{C}$ experiment mentioned previously that was used to independently verify the ANC for $^{14}C + n \leftrightarrow ^{15}C$.

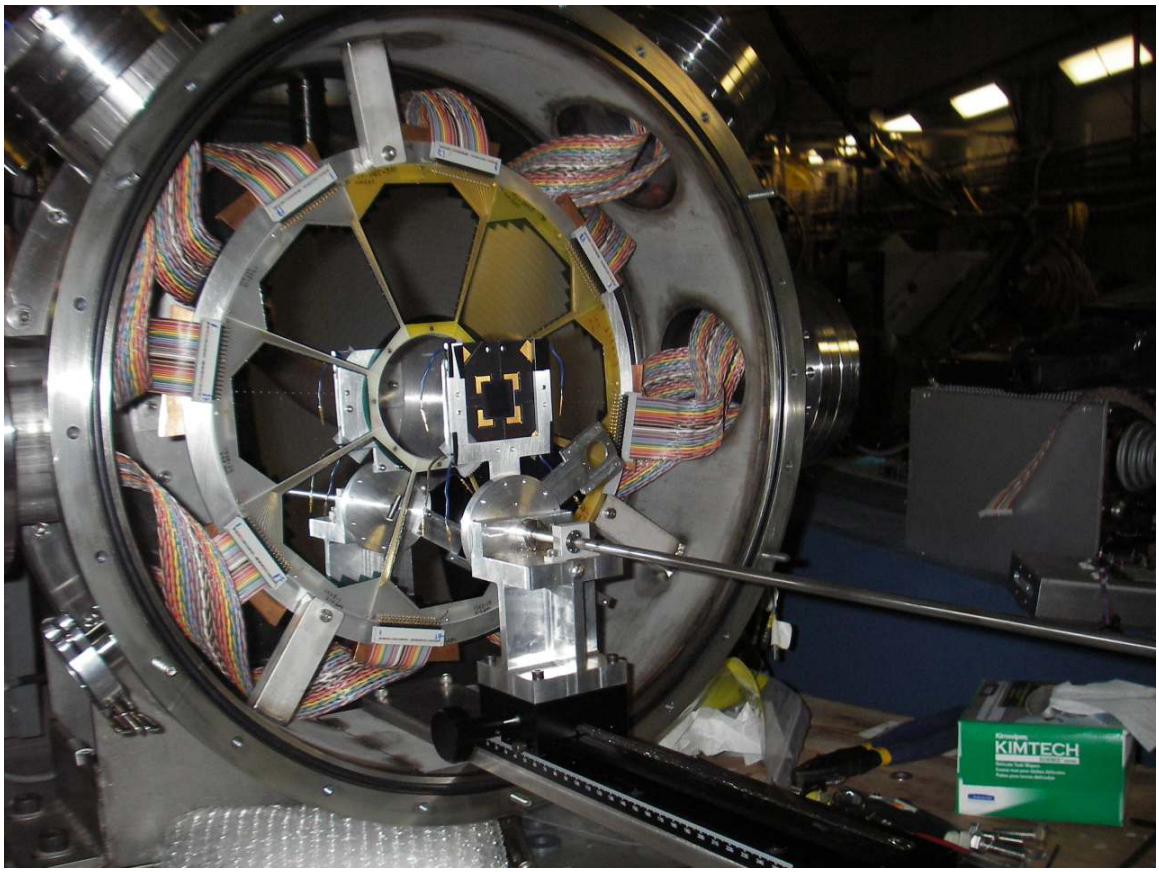

Fig. 8. The TECSA silicon detector array. Target chamber has been removed for a better view.

CHAPTER IV

DATA ANALYSIS

The data analysis is divided into two parts. First, the ANC for $^{15}C \leftrightarrow ^{14}C+n$ is determined. This primarily involves the analysis of the heavy ion (HI) neutron transfer reaction $^{13}C(^{14}C,^{15}C)^{12}C$. Additionally, the inverse kinematics reaction $d(^{14}C,p)^{15}C$ measured using TECSA was used to verify the result. The second part of the analysis then uses this ANC in an attempt to find the SF for the configuration $(^{14}C+n)_{gnd}$ in ^{15}C.

A. ANC for $^{15}C \leftrightarrow ^{14}C+n$

1. $^{13}C(^{14}C,^{15}C)^{12}C$

In this experiment a 12 MeV/nucleon ^{14}C beam impinged on a ^{13}C target. Reaction products were measured using the MDM spectrometer and the Oxford detector. Because of similar Bρ values for the elastically scattered particles and the neutron transfer reaction products, both elastic scattering and transfer were able to be measured simultaneously. Particle identification was made by plotting the energy loss in the gas against the energy deposited when stopping in the scintillator, as shown in Fig. 5, and polygon gate conditions were set around the elastic and transfer peaks. Reaction products were measured with the MDM spectrometer at 4°, 6°, 9°, 12° and 15°, each spectrometer setting used the 4° x 1° mask, allowing overlap to check for consistency. Because of low cross sections at larger angles, only elastic scattering was measured at 15°. Limited beam time in conjunction with the lower cross sections at larger angles limited the angular range of the measured elastic scattering more than would be ideal, as will be apparent in the discussion of the optical model fits.

Target thickness was measured offline using a ^{228}Th α source. Both the Au and ^{13}C targets were placed onto a ladder attached to a linear motion vacuum feed through, as was an empty frame. This ladder was then placed between the source and a 1mm thick silicon detector. The silicon detector was connected through a preamplifier to a shaping amplifier whose output

was digitized and recorded using a multichannel analyzer (MCA). The ^{228}Th spectrum was measured with the empty frame in place and then the spectrum was again measured with the Au and then the ^{13}C targets. A calibration was performed for the spectrum taken with the empty frame and then the shift of the peaks with the other targets was measured. The energy shifts of five of the α peaks in the ^{228}Th spectrum were then compared with energy loss calculations performed using LISE [36]. The thickness of the ^{13}C target was found to be 101 μg/cm^2 ± 4 μg/cm^2.

The target angle was reconstructed as described in the previous chapter. It was checked with the five finger mask with the spectrometer at 4°. Comparison of the positions of the reconstructed target angles with the known angles of the slits of the mask gave a second order polynomial correction function for the target angle that was used for all spectrometer angles. The validity of this correction was checked by observing that the high and low angle cutoffs in the reconstructed target angle corresponded to the known edges of the 4°x1° mask. The solid angle of the 4°x1° mask was calculated using the formula:

$$\Omega = \iint_s \frac{\hat{n} \bullet d\vec{a}}{r^2} \tag{4.1}$$

where $\hat{n}$ is a unit vector that points in the direction from the center of the target to the area segment $d\vec{a}$. The distance from the target to the area segment of the slit is r and s denotes integration over the surface of the slit.

Using the polygon gate condition shown in Fig. 5, the position in the focal plane of elastic (or transfer) particles is plotted against the (corrected) reconstructed target angle (Fig. 9). The position in the focal plane depends on the energy of the particle and can be calculated using RAYTRACE. Inside the particle ID gate for ^{14}C are both elastic and inelastic scattering, and therefore another polygon gate is placed around the elastic scattering. This is then projected onto the target angle axis and divided into 16 bins 0.25° in width, which gives the angular distribution for this spectrometer setting.

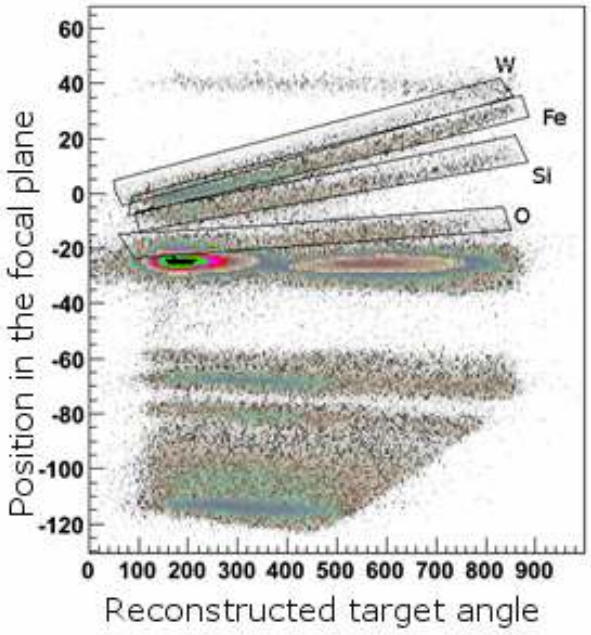

Fig. 9. The contents of the elastic gate, which was shown in Fig. 5, is plotted in position in focal plane against reconstructed target angle. Peaks from scattering on impurities in the target are labeled.

Normalization of the measured angular distribution into a differential cross section is given by

$$\frac{d\sigma}{d\Omega}(\theta) = \frac{N_{det}}{N_{inc} N_t \Delta\Omega}, \tag{4.2}$$

where N_{det} is the number of particles detected in solid angle $\Delta\Omega$ at angle θ for N_{inc} number of particles incident on a target that is N_t atoms/cm^2 thick. Differential cross sections are typically given in millibarns/steradian (mb/sr) where 1 mb = 1x10^{-27} cm^2. The number of particles incident on the target is determined by the integration of the beam current in the Faraday cup after the target. A correction for the dead time of the data acquisition system is also applied.

Elastic scattering on several impurities in the target can be seen in Fig. 9. The impurities are identified by comparing the location of the focal plane of particles scattered off of them and also their x position in the focal plane with RAYTRACE calculations. At small angles the scattering on impurities cannot be distinguished from scattering on ^{13}C and therefore it is important to estimate the contribution of the impurities at these small angles. For scattering on the heavier impurities such as W, Fe and Si at small angles, the scattering should basically be Rutherford, however at larger angles (for Fe above about 4° in this case and for Si sooner) the cross sections may deviate significantly from that of Rutherford scattering. Therefore, to estimate the contribution of these impurities at small angles their angular distributions were

measured at larger angles where they were well separated from the scattering on ^{13}C. The angular distributions were then compared with optical model calculations using a potential generated by a double folding procedure using generic normalizations and ranges. The data were then normalized to the calculations to find the amount of each impurity in the target. The most significant were Fe (1%), Si (0.4%) and O (2.7%). Using the calculated angular distributions and the normalized measured angular distributions at larger angles the contributions at forward angles were estimated and corrections were made for them.

Optical model fits

The elastic scattering data were used to find a suitable OMP that could be used for the transfer DWBA calculation. An optical potential of the form of (2.25) was used, however the imaginary surface and spin orbit interactions were neglected as a good fit was possible without them and adding them would greatly increase the number of parameters and thus the complexity of the fitting procedure. Calculation of the elastic scattering and fitting to the experimental data were performed using the optical model elastic scattering code OPTIMINIX [37] and also in PTOLEMY [38]. Both of these codes are solving the Schrödinger equation that describes the relative motion, using the user-specified potential, and calculating the differential cross section from the resulting wave function. The codes have the option, used here, to read in experimental scattering data and associated uncertainty to which they fit, using a χ^2 minimization routine, the calculated distribution by varying the parameters specified as free by the user. A grid search was performed in V, the depth of the real potential, while allowing the other five parameters to be fit for each point. The results, shown in Fig. 10, indicate a highly ambiguous solution with some discrete ambiguities for low V, and continuously ambiguous beyond about 100 MeV. Since it was apparent that practically any V could produce an acceptable fit, several were selected for further fitting.

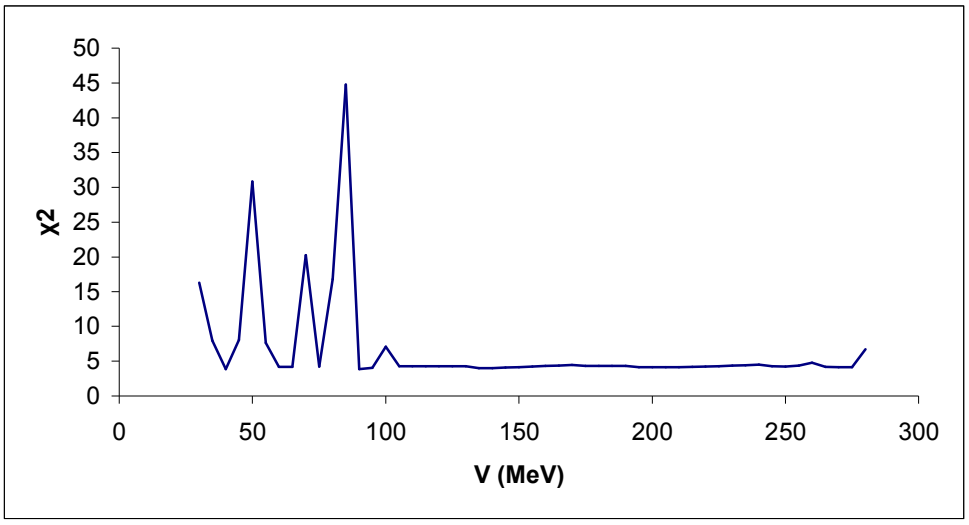

Figure 10. Grid search in V for elastic scattering of ^{14}C on ^{13}C.

For each of the five selected WS potentials another fit was then performed allowing all six parameters to be optimized. The results are summarized in Table 2. The real depth, V, and correspondingly the real volume potential varies greatly, while the imaginary depth, W, is nearly constant at around 15 MeV. Each potential gives a good fit to the elastic scattering data. In Table 2, $r_{v(w)}$ and $a_{v(w)}$ are the real (imaginary) radius parameter and diffuseness respectively, χ^2 is given by

$$\chi^2 = \frac{1}{N-f}\sum_i \frac{(\sigma_{exp}(\theta_i)-\sigma_{theory}(\theta_i))^2}{(\delta\sigma_{exp}(\theta_i))^2}, \tag{4.3}$$

where N is the number of data points, f is the number of free parameters and $\delta\sigma_{exp}(\theta_i)$ is the experimental uncertainty of data point i. J_v and J_w are the volume integrals per nucleon pair defined as

$$J = J_v + iJ_w = -\frac{4\pi}{A_p A_t}\int_0^\infty (V(r)+iW(r))r^2\,dr\,. \tag{4.4}$$

The real volume integral varies significantly as is expected for the large range of V, while the imaginary volume integral varies little. The mean squared radii are given in the columns labeled R_v and R_w.

Table 2. Optical model potential parameters for 12 MeV/nucleon ^{14}C elastic on ^{13}C.

	V (MeV)	W (MeV)	r_v (fm)	r_w (fm)	a_v (fm)	a_w (fm)	χ^2	J_v (MeV fm^3)	R_v (fm)	J_w (MeV fm^3)	R_w (fm)
WS1	77.1	13.32	0.987	1.209	0.703	0.723	3.09	225	4.480	68	5.206
WS2	118.7	14.15	0.927	1.191	0.690	0.739	3.4	292	4.275	69	5.182
WS3	162.4	15.03	0.891	1.169	0.674	0.767	3.59	357	4.132	71	5.169
WS4	203.1	16.04	0.894	1.133	0.627	0.825	3.6	438	4.038	71	5.183
WS5	248.8	16.66	0.885	1.115	0.606	0.848	3.65	516	3.965	72	5.180

The real potentials are plotted in Fig. 11 as a function of radius. While the depths at r=0 vary significantly, the potentials are similar in the surface region (around 5 to 9 fm), which is where the peripheral transfer reaction is expected to take place. The radial dependence of the calculation was evaluated by placing a Gaussian perturbation at various radii and recording the χ^2 for each point. The result of this test is shown in Fig. 12. The strongest radial dependence is from about 5.5 to 7.5 fm, with a much less significant effect at smaller radii. Angular distributions from four of the potentials are shown in Fig. 13, and a reasonable agreement with the data for the substantially different potentials is evident, which highlights the ambiguous nature of optical potentials fit to elastic scattering. Also shown in Fig. 13 is a decomposition of the angular distribution into near- and far-side components. An interesting feature of the calculations is the peak in the far-side component at around 45°, however no reliable data were obtained at these larger angles to compare with the calculation. This is an example of the ambiguity inherent in these calculations, particularly when too little data are available.

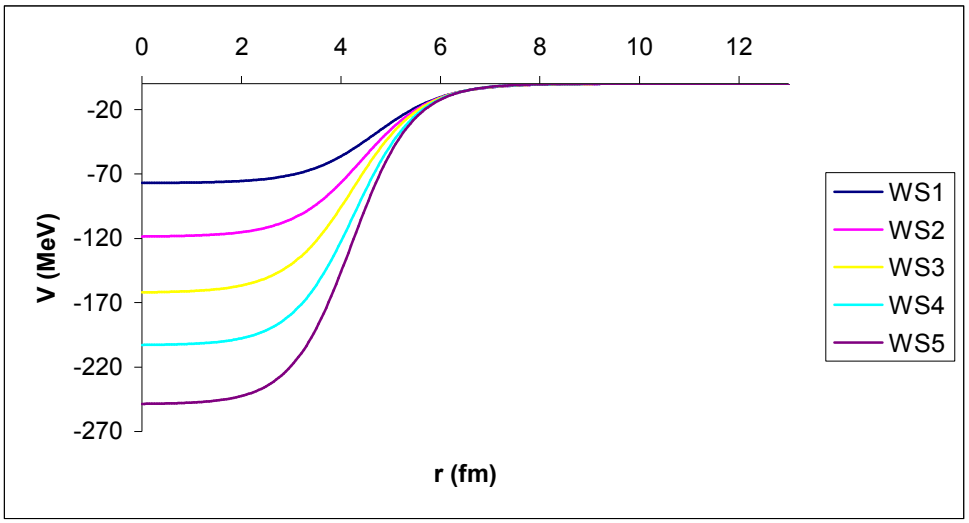

Fig. 11. Real part of the potential as a function of radius. Note the convergence in the surface region.

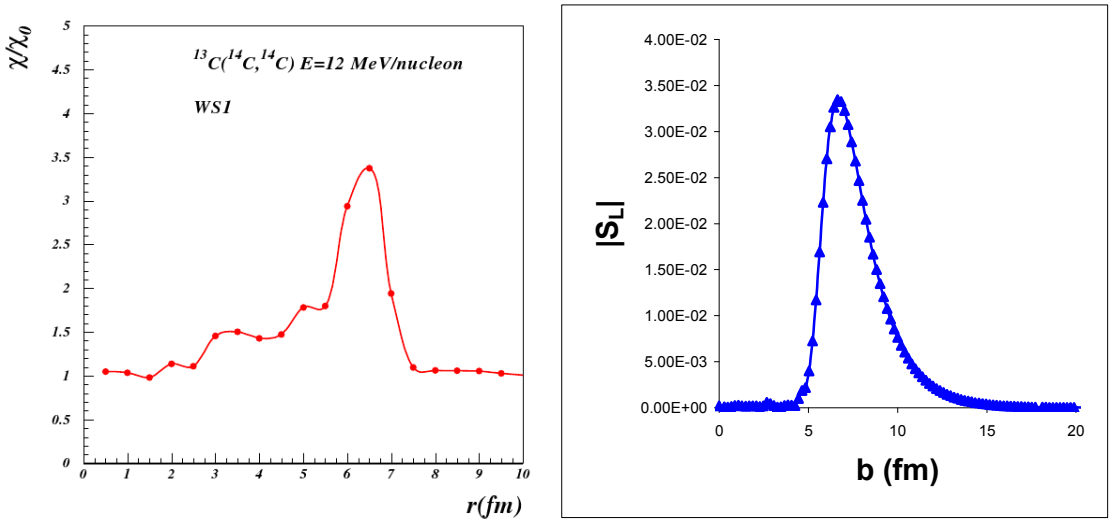

Fig. 12. On the left is the effect on the χ^2 of a Gaussian perturbation placed at different radii for the WS1 OMP. On the right is the transfer S-matrix as function of impact parameter for the DF OMP, showing that most of its peak is well into the surface region (~6 fm).

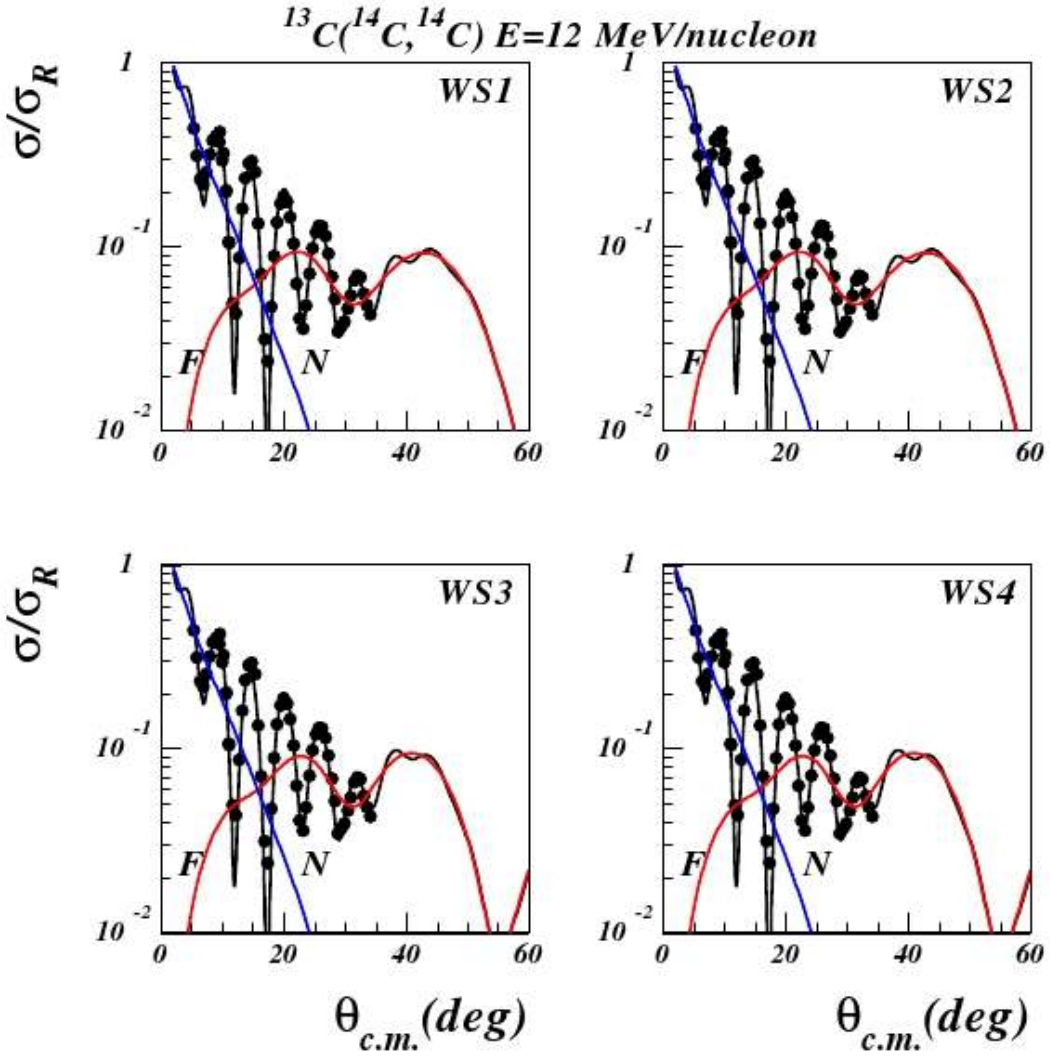

Fig. 13. Experimental data points are shown as black dots. Also shown are the calculated near (blue line) and far (red line) distributions and their coherent sum (black line).

Double folding

An alternative approach, the double folding (DF) method with the JLM effective interaction described in Ch. 2, was also used to obtain an optical potential for the ^{14}C + ^{13}C elastic channel. The average values N_v=0.37, N_w=1.0 for the normalizations found in [28] were used as a starting point for the calculations. A reasonable fit to the data (reduced χ^2=3.4) was obtained with N_v=0.45, N_w=0.9, t_v=1.2 and t_w=1.75 and is shown in Fig. 14. A smearing routine

was applied to the calculation to reflect the angular resolution of the detector that was observed with the five finger mask ($\delta\theta$=0.30° C.M). A near and far side decomposition of the calculation is shown in Fig. 15. The higher angle peak in the far side component is absent for this potential.

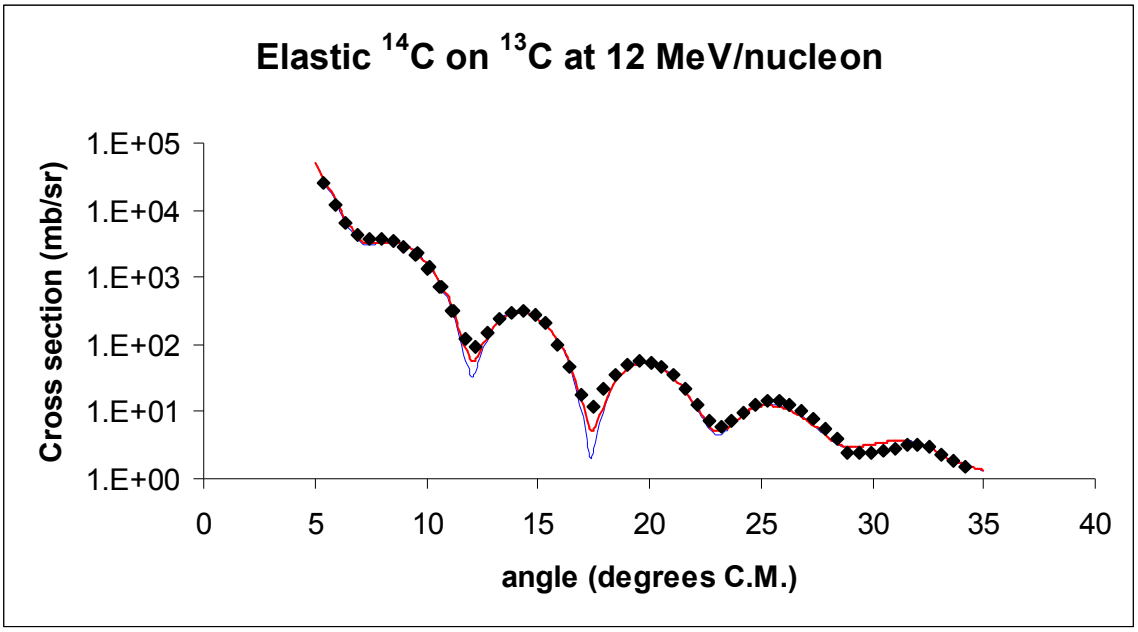

Fig. 14. Experimental points are the black dots. The blue and red lines are the optical model calculations obtained with the double folding procedure before and after, respectively, smearing to reflect the experimental angular resolution of the detector.

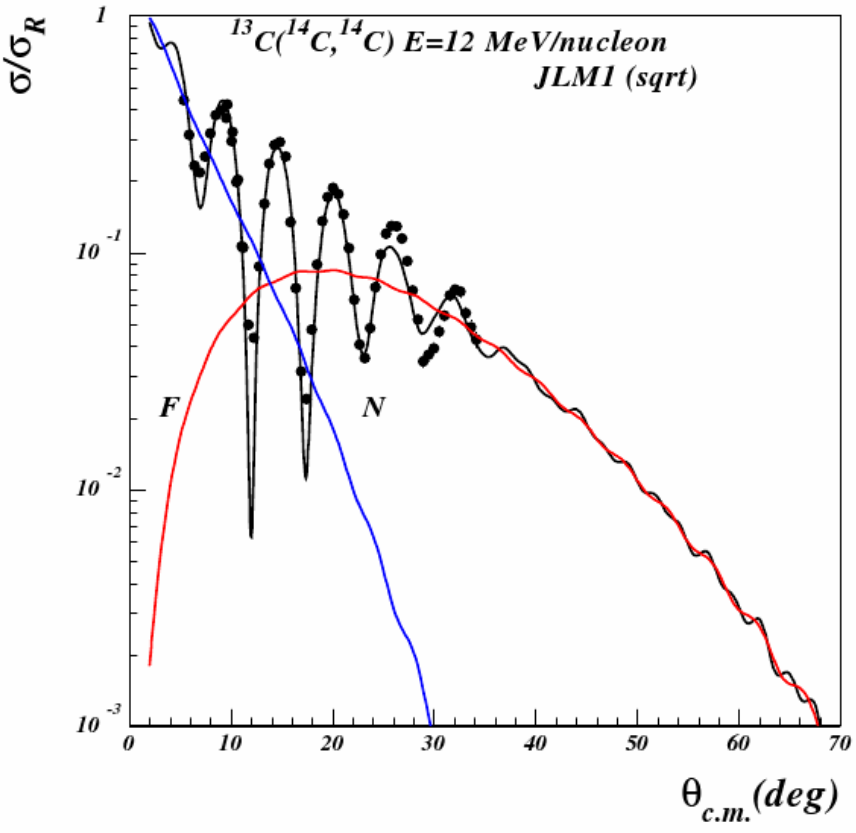

Fig. 15. Double folding potential near/far decomposition.

Transfer

The angular distribution for the HI neutron transfer reaction was measured for the ^{15}C ground state ($J^{\pi}=1/2^{+}$) and first excited state (E_{exc}=740 keV, $J^{\pi}=5/2^{+}$) from about 5° to 30° C.M. An example of a transfer distribution is shown in Fig. 16, with data taken from the gate labeled "transfer" in Fig. 8. Because of the proximity and low counts in the ground state peak, a fit of the ground state and first excited state to Gaussian peaks was performed in ROOT [39]. The resulting functions were then integrated to get the counts in each peak. An example of such a fit is shown in Fig. 17.

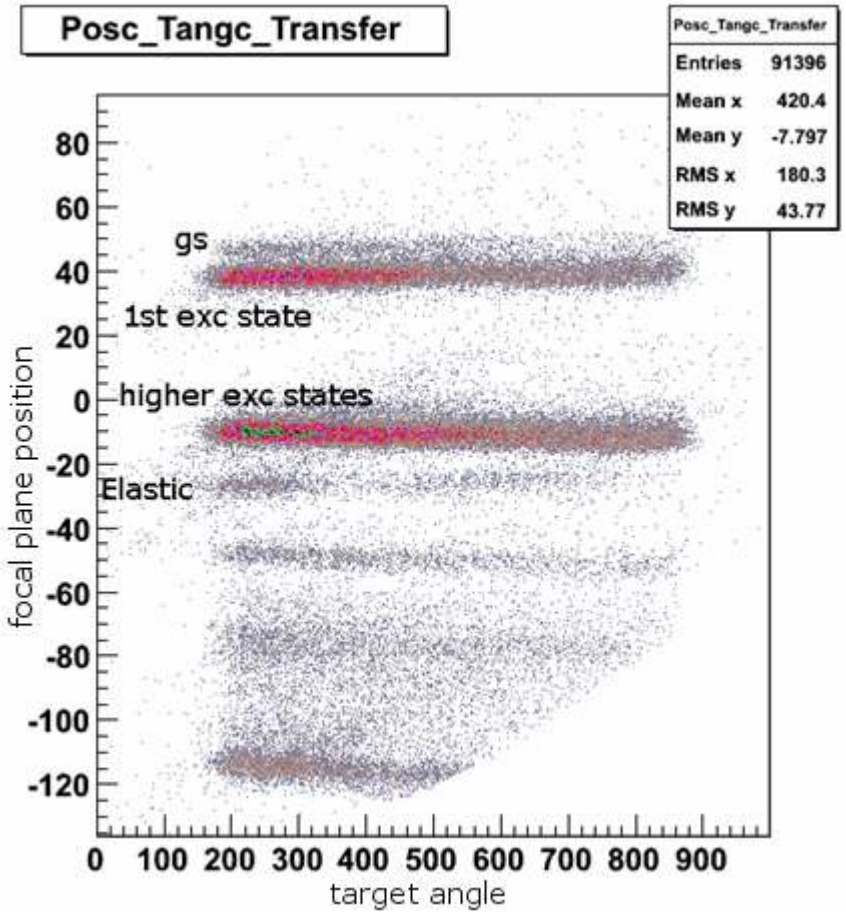

Fig. 16. Position in the focal plane vs reconstructed target angle.

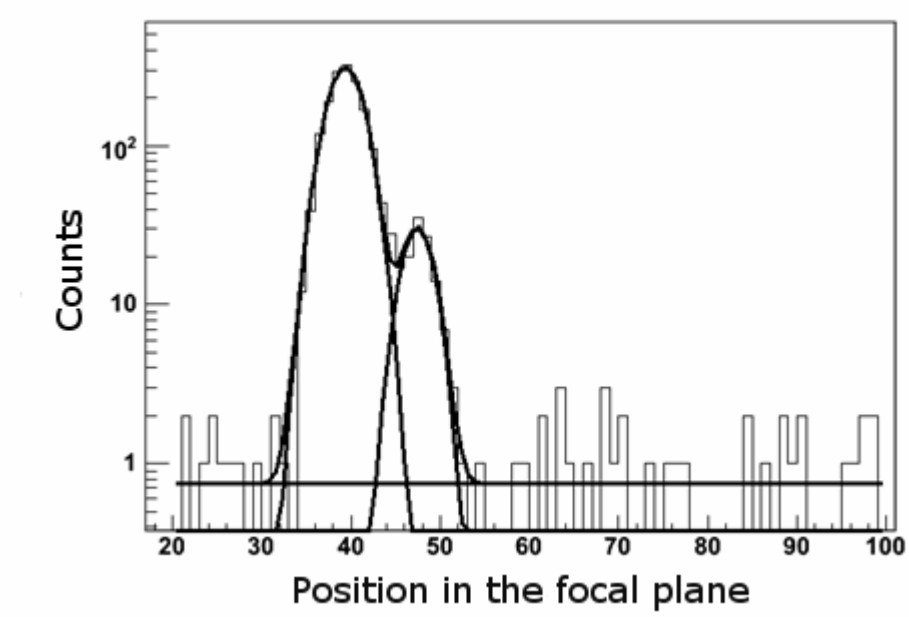

Fig. 17. An example of a fit of Gaussian functions to the ground state and first excited state of ^{15}C, plus a linear background.

DWBA calculations were performed using the code PTOLEMY with the optical potentials obtained by fits to the elastic scattering as input. Using the OMP, PTOLEMY solves the Schrödinger equation describing the scattering problem and computes the S-matrix for the user-specified range of orbital angular momentum values. The calculation of the wave functions is controlled by the choice of step size and radial cutoff (given in fm), which can be specified by using a built-in parameter set or be explicitly given. It is important to vary these values to check for convergence. With the wave functions calculated, PTOLEMY then computes the radial integrals for the transfer reaction and calculates the angular distribution for the cross section, again using a user-specified or built in parameter set to control the integration grid. For all the calculations shown here, these parameter values were varied in order to confirm convergence and stability in the calculated angular distribution for a given potential input. For each calculation the same potential was used for both the entrance and exit channels. In the case of the potential obtained through the double folding procedure, the real and imaginary parts of the potential were fit to a Woods-Saxon (WS) form over the surface region (3 to 9 fm) to obtain a potential to be used in the PTOLEMY DWBA calculation. The results of the calculations are shown in Fig. 18 and Fig. 19. The same calculation was performed for the $5/2^+$ first excited state and the results for that are plotted in Fig. 20. While the calculated angular distributions vary

significantly at larger angles, they agree reasonably well up to the first observed minimum around 12°. The reactions leading to a ^{15}C exiting the target at larger angles are associated with smaller impact parameters and therefore may not be described well by the DWBA since other reaction channels may have a non-trivial influence. Perhaps more significantly, these reactions take place further into the interior of the nucleus at a radius that the elastic scattering is not sensitive to (see Fig. 12). The calculations were normalized to the experimental angular distribution to obtain the phenomenological SF.

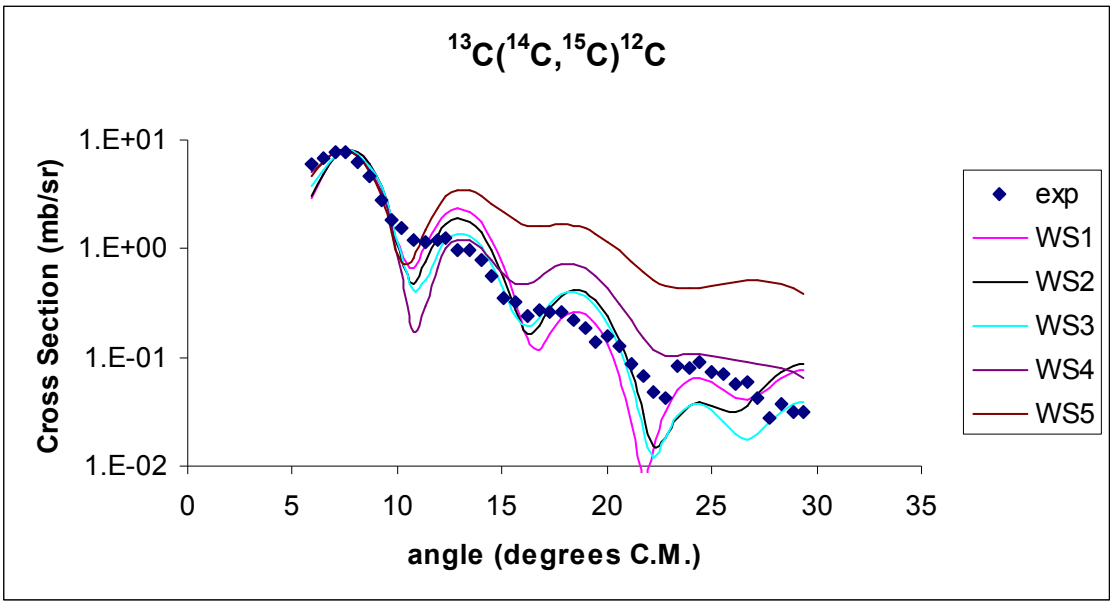

Fig. 18. The calculated distributions for the ground state have been normalized to the experimental data from 5 to 11°.

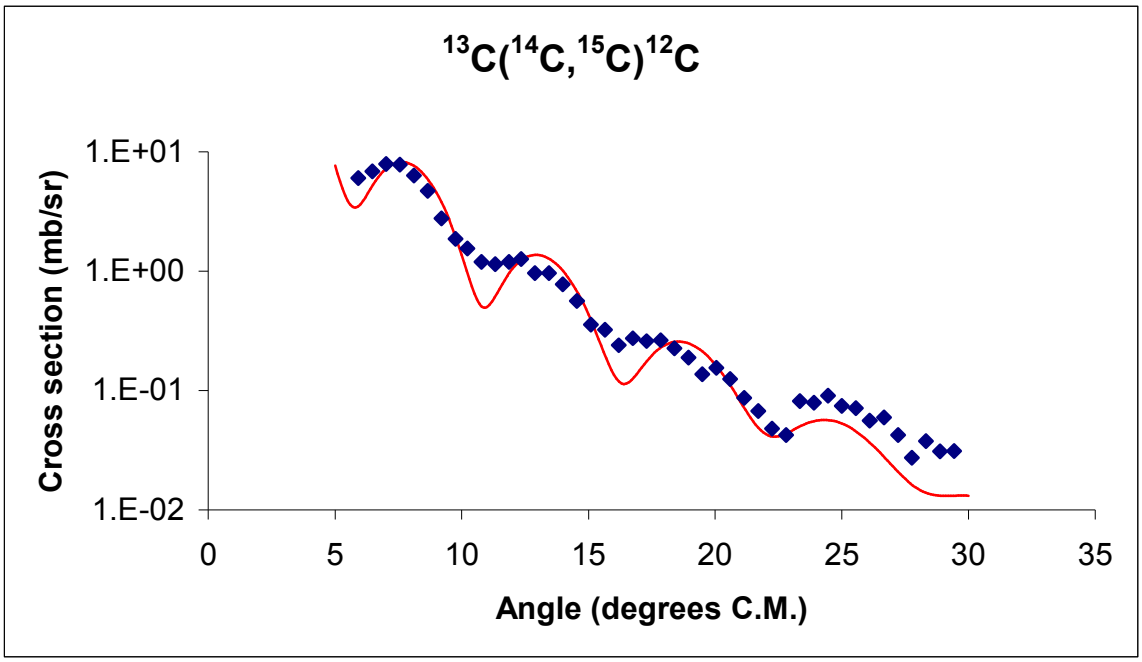

Fig. 19. Double folding potential normalized to experimental distribution for the ground state.

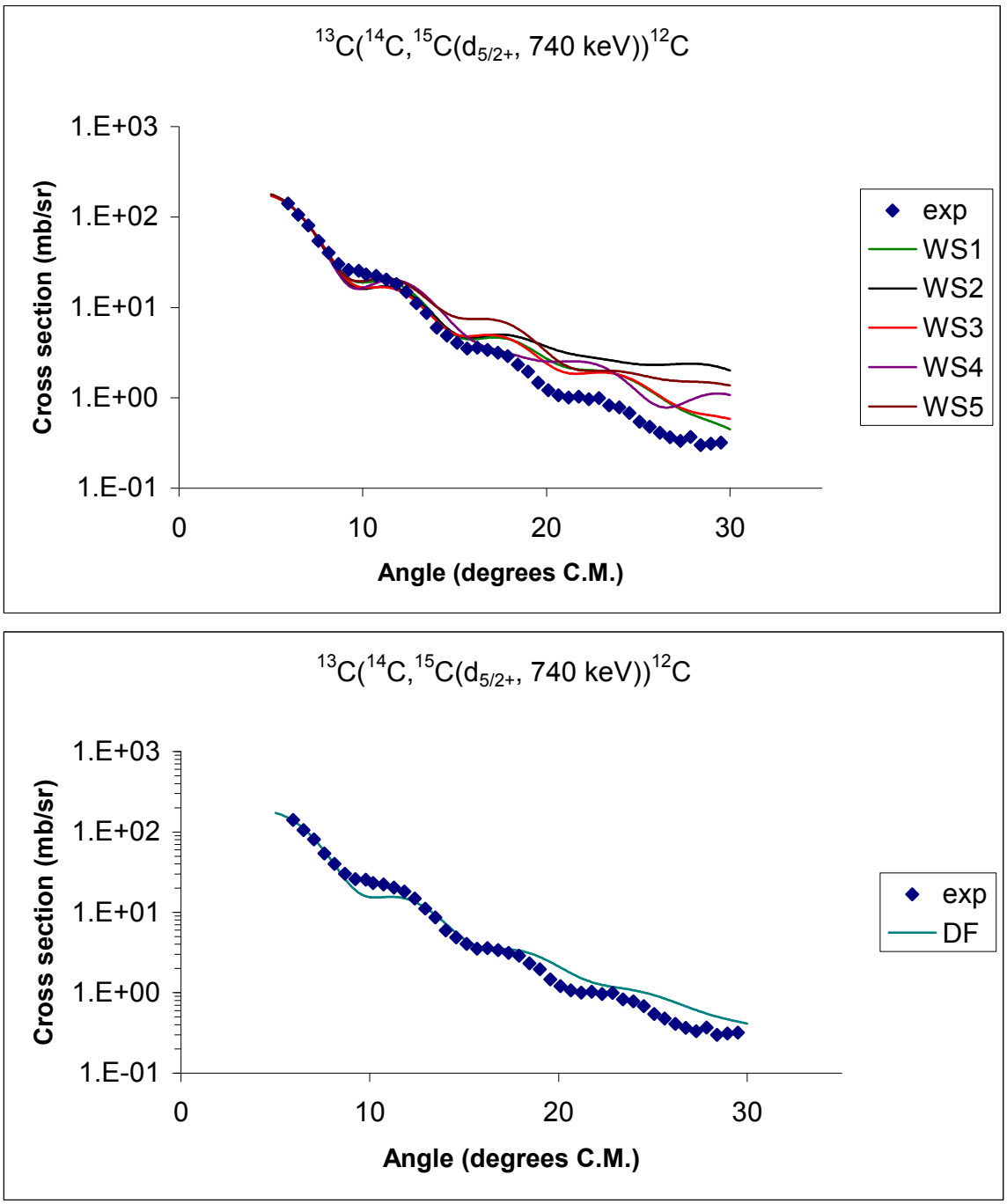

Fig. 20. Angular distribution for the first excited state, shown with calculations (WS potentials from the grid search top, DF bottom) which have be normalized to the experiment.

The single particle ANC is given by [6]

$$b_{lj} \underset{r>R}{=} \frac{\varphi_{nlj}}{h_l(2\kappa r) r^{-1}} . \tag{4.5}$$

In this case, $l = 0$ for capture to the $2s_{1/2}$ ground state. Equation (4.5) holds for values of r well outside of the nuclear radius R. The wave function calculated by PTOLEMY divided by the Hankel function over r was plotted as a function of the radius and the value of this function in the asymptotic region where it is flat is the SPANC (see Fig. 21). This was performed for both ^{13}C and ^{15}C. The ANC can be determined by (2.42) given knowledge of the ANC^2 for $^{13}C \leftrightarrow {}^{12}C+n$, which is $C^2_{(1p_{1/2},{}^{13}C)} = 2.31 \pm 0.08$ fm^{-1} [40]. The ANC for $^{15}C \leftrightarrow {}^{14}C+n$ determined from the WS and DF fits are given in Table 3. The same procedure was also applied to the neutron transfer to the $5/2^+$ state in ^{15}C. The angular distribution and the fits are shown in Fig. 20, normalized to the experimental data in most forward peak of the distribution. The extracted values for $C^2_{d5/2}$ are summarized in the last column in Table 3.

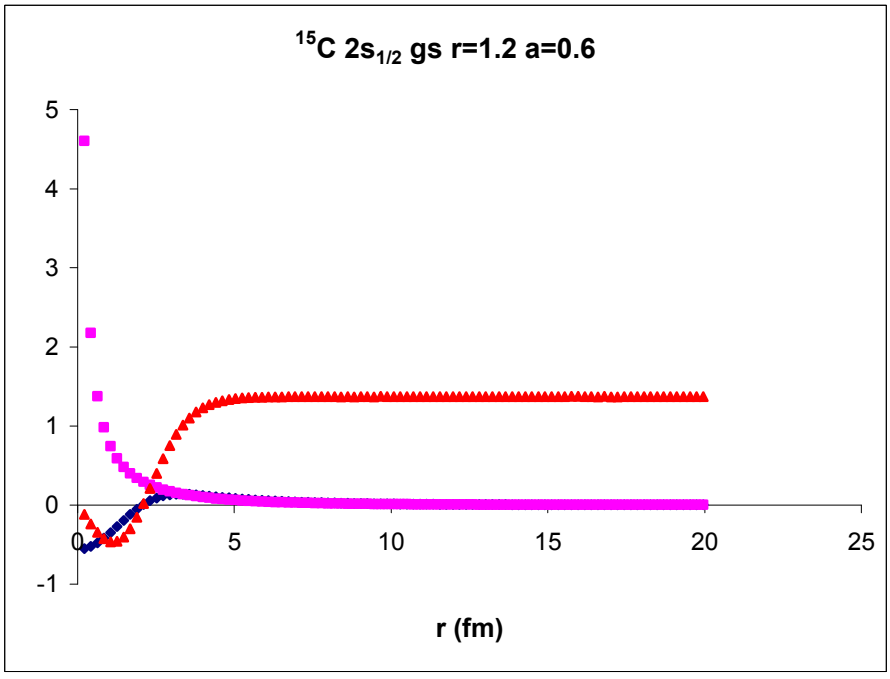

Fig. 21. The blue diamonds are the calculated wave function, the magenta squares are the Hankel function, and the red triangles are the ratio between the two, which in the asymptotic region (beyond about 9 fm where it is flat) is equal to the single particle ANC for ^{15}C ($b_{2s1/2}$=1.37 fm-1/2) with r_0=1.2 fm and a=0.60 fm.

Table 3. Normalizations (N) and ANCs obtained with DWBA calculation using the WS OMP fits.

	$SF_{2s1/2}$	$C^2_{2s_{1/2}}$ (fm^{-1})	$SF_{1d5/2}$	$C^2_{1d_{5/2}}$ x10^{-3} (fm^{-1})
WS1-WS1	1.22	2.30	1.13	4.45
WS2-WS2	1.16	2.18	1.02	4.03
WS3-WS3	1.04	1.95	1.13	4.46
WS4-WS4	0.98	1.83	1.20	4.74
WS5-WS5	1.14	2.14	1.25	4.94
DF	1.15	2.16	1.09	4.28
Average	1.12	**2.09**	1.14	**4.48**

The sources of uncertainty in the ANCs for the gs were as follows: 4% target thickness, 3% normalization to the number of incident particles, 5% data extraction and disentanglement from the 1st excited state of ^{15}C, 6% statistical uncertainty and 10% systematic uncertainty based on the variation of the results from the calculations. Adding these independent sources of uncertainty in quadrature gives an overall uncertainty in the C^2 of 14%, and thus $C^2_{2s_{1/2}} = 2.09 \pm 0.29$ fm^{-1}. The first excited state had lower statistical uncertainty, around 1% at the forward angles, giving an overall uncertainty for its ANC^2 of 13% and therefore $C^2_{1d_{5/2}} = (4.48 \pm 0.58) \bullet 10^{-3}$ fm^{-1}.

2. $d(^{14}C,p)^{15}C$

The $^{14}C(d,p)^{15}C$ reaction was measured in inverse kinematics with an 11.7 MeV/nucleon ^{14}C beam on a deuterated polyethelyne target using the TECSA detector array mounted on the MARS beam line at Texas A&M, as described in the previous chapter. The 3^+ beam from the K500 cyclotron was fully stripped by a foil after extraction in order to remove the ^{14}N impurity. MARS was used with no target at the primary (production) target position, allowing the ^{14}C beam to simply pass through MARS to the secondary target position, where TECSA was mounted. The TECSA target thickness was 251 ± 5 μg/cm^2 with a deuterium:hydrogen ratio of 98:2. The detector array was mounted in the backward (lab) direction and protons from the reaction were measured (see Fig. 7). The reaction was measured with the distance from the target to the detector array at 20, 12, 5 and 2.8 cm covering an angular range of 102° to 165° lab (4.5°

to 32.2° CM) with overlap to check for consistency. The reaction rate was normalized to the incident beam measured in a Faraday cup immediately behind the target.

An adiabatic distorted wave approximation calculation (ADWA) was made using potentials taken from the CH89 [41] parameterization. In the ADWA the breakup of the deuteron in the entrance channel is handled explicitly and the transition matrix for a (*d*,*p*) reaction

$$\tilde{T} = \langle \chi^{(-)} \phi_{nA} \mid V_{np} \mid \Psi^{(+)} \rangle \tag{4.6}$$

reduces to [42]

$$\tilde{T}_{ADW} = \langle \chi^{(-)} \phi_{nA} \mid V_{pn} \mid \tilde{\chi} \phi_{pn} \rangle , \tag{4.7}$$

where the *n*-*p* effective interaction, V_{pn}, is taken to be zero range and

$$[E + \epsilon_0 - T_R - \bar{V}]\tilde{\chi} = 0 . \tag{4.8}$$

Here ϵ_0 is the deuteron binding energy and

$$\bar{V} = V_n + V_p + V_C , \tag{4.9}$$

where V_n and V_p are, respectively, the neutron and proton optical potentials evaluated at half of the deuteron energy. V_C is the Coulomb potential. Finite range effects on the deuteron potential can be approximated by [43]

$$U_{FR} \approx \frac{\langle \phi_d \mid V_{np}(V_n + V_p) \mid \phi_d \rangle}{\langle \phi_d \mid V_{pn} \mid \phi_d \rangle} . \tag{4.10}$$

This potential still contains the proton- and neutron-target optical potentials evaluated at half the deuteron energy, but the evaluation is significantly more complex, requiring integration over the deuteron wave function along with the *n*-*p* interaction. A simple approximation of the finite range effect was given by Ref. [44] and this, along with the formulation of Ref. [43], were examined for several cases in [45]. For both approximations an increase in real and imaginary diffuseness and real and imaginary depths was observed, though the two approximations differed in amount. For all ADWA calculations performed here the Wales-Johnson approximation of [44] was used for simplicity of calculation.

The ADWA has the advantage that only nucleon optical potentials are required, for which CH89 was utilized. The Reid soft core potential [46] was used for the *n*-*p* interaction. The calculations were made using the coupled-channel reaction code FRESCO [47]. The experimental angular distribution and calculation for the transfer to the ground state and first excited state are shown in Fig. 22.

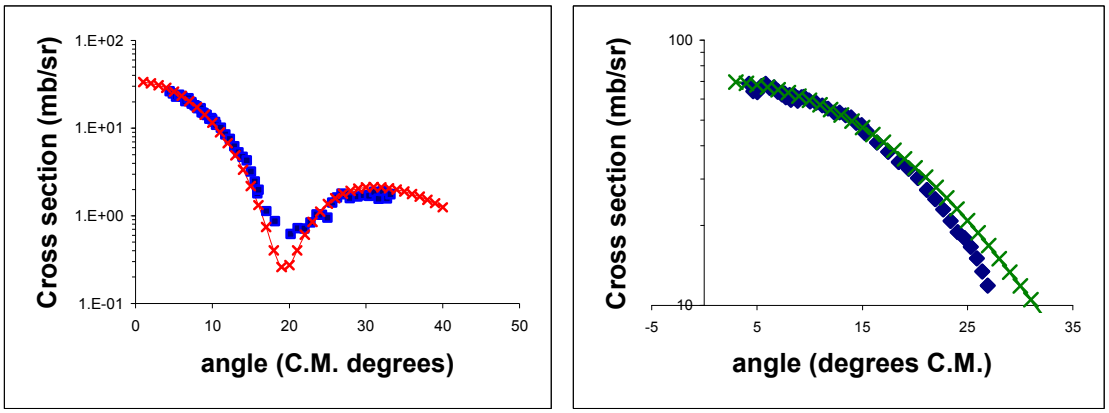

Fig. 22. On the left is the transfer to the $2s_{1/2}$ ground state. Blue squares mark the experimental data points and the red line is the ADWA calculation. On the right is the 740 keV $1d_{5/2}$ first excited state, with experimental points shown as blue squares and the ADWA calculation as a green line.

The overall experimental uncertainty for the measured differential cross section was 8%, which consisted of 2% due to target thickness, 2% incident beam normalization, 4% for the analysis and < 2% for statistics. This combined with a 10% systematic uncertainty gives an overall error in C^2 of 12%. C^2 for the ground state was found to be $C^2_{2s_{1/2}}=2.01\pm0.24$ fm^{-1} and the first excited state $C^2_{1d_{5/2}}=(4.06\pm0.49)\bullet10^{-3}$ fm^{-1}.

B. Non-peripheral ^{14}C(d,p)^{15}C

For this experiment a 60 MeV deuteron beam was used on a high-purity ^{14}C target. The incident deuteron energy of 60 MeV was selected to be a compromise between penetration into the interior of the nucleus to maximize the contribution of that region to the transfer matrix element and the low cross section at higher energies that results from a large momentum mismatch for the proton between the entrance and exit channels. Target thickness was determined online using a 15 MeV/nucleon ^{20}Ne beam on the ^{14}C target backed by a ~600 μg/cm^2 Au target. The single slit collimator was used and the position of the peak in the focal plane of the spectrometer was measured. This was repeated for several different positions on the target to check for uniformity. After the position in the FP had been measured for the different spots on the target, the ^{14}C target was removed and the position in the focal plane was again measured. By comparing the shift to a calculation with RAYTRACE the thickness was

determined for each position on the target that was measured. The thickness for the ^{14}C target was found to be 355 ± 25 μg/cm^2. During the experiment (*d*,*p*) was measured on a ^{12}C target of known thickness as well and this was compared with the measured ^{12}C(*d*,*p*) from impurity in the ^{14}C target to determine the amount of ^{12}C in the ^{14}C target. The ^{14}C target was found to have approximately 1.6x10^{18} atoms/cm^2 ^{12}C, or about 11% by number. Elastic scattering on the ^{12}C target was also measured and this was used to correct the elastic angular distribution for scattering on ^{14}C.

The angular distributions for both elastic scattering and (*d*,*p*) on the ^{14}C target were measured. As noted in Ch. 3, particle identification was made using only a thick scintillator because of the low energy deposited in the isobutane gas by the light, high energy particles. Particle identification and the proton spectrum are shown in Fig. 23.

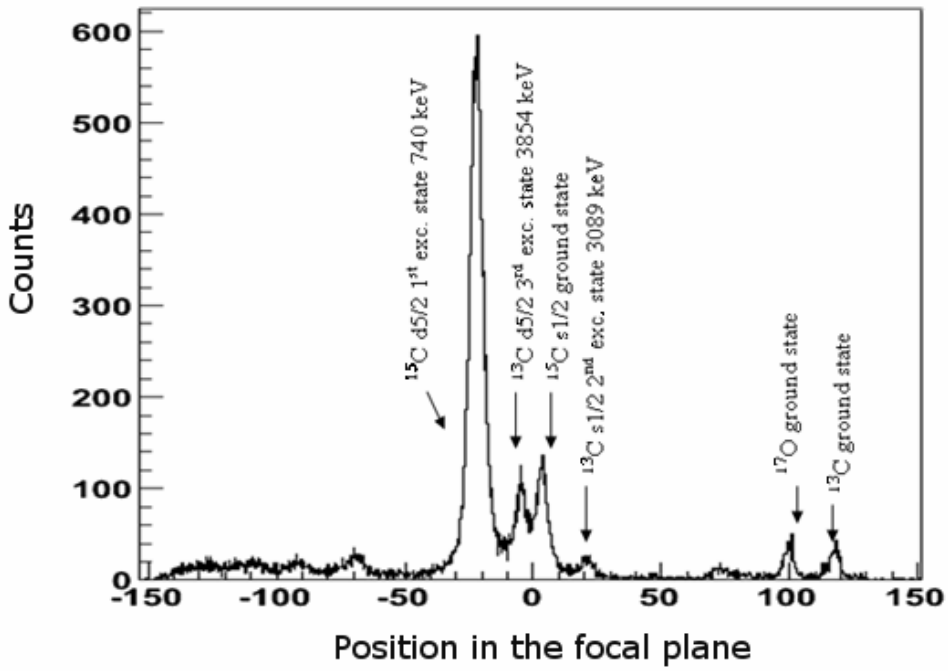

Fig. 23. This histogram shows the content of the proton peak on the right in Fig. 6 plotted as a function of position in the focal plane.

The elastic scattering was fit using an OMP of the WS form. The global potential parameterization of [48] was used as a seed. To improve the fit, spin orbit coupling and the surface imaginary terms were neglected. A grid search for values of the real volume potential

was performed to find local χ^2 minima (Fig. 24). The local minima were then used for a further fit over all six optical model parameters. The three fits are shown in Fig. 25. The potential parameters are given in Table 4.

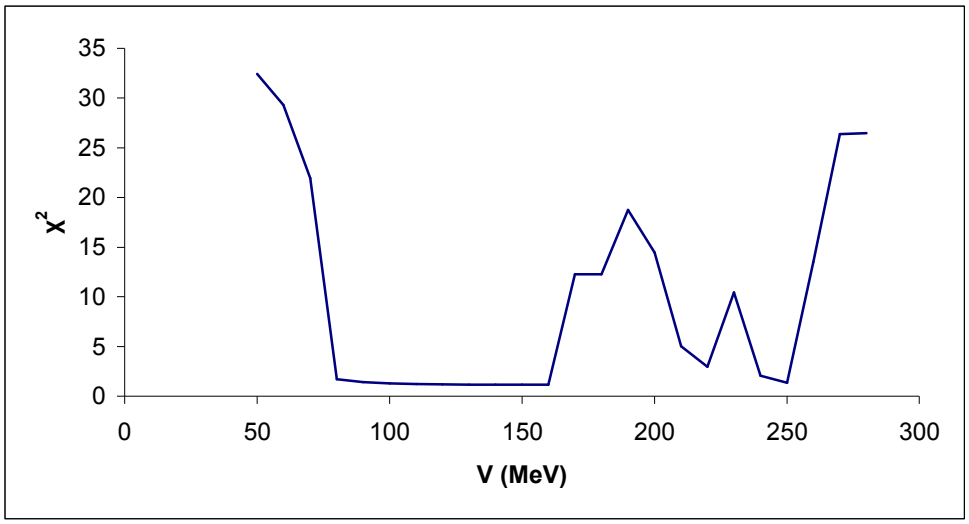

Fig. 24. Grid search in V.

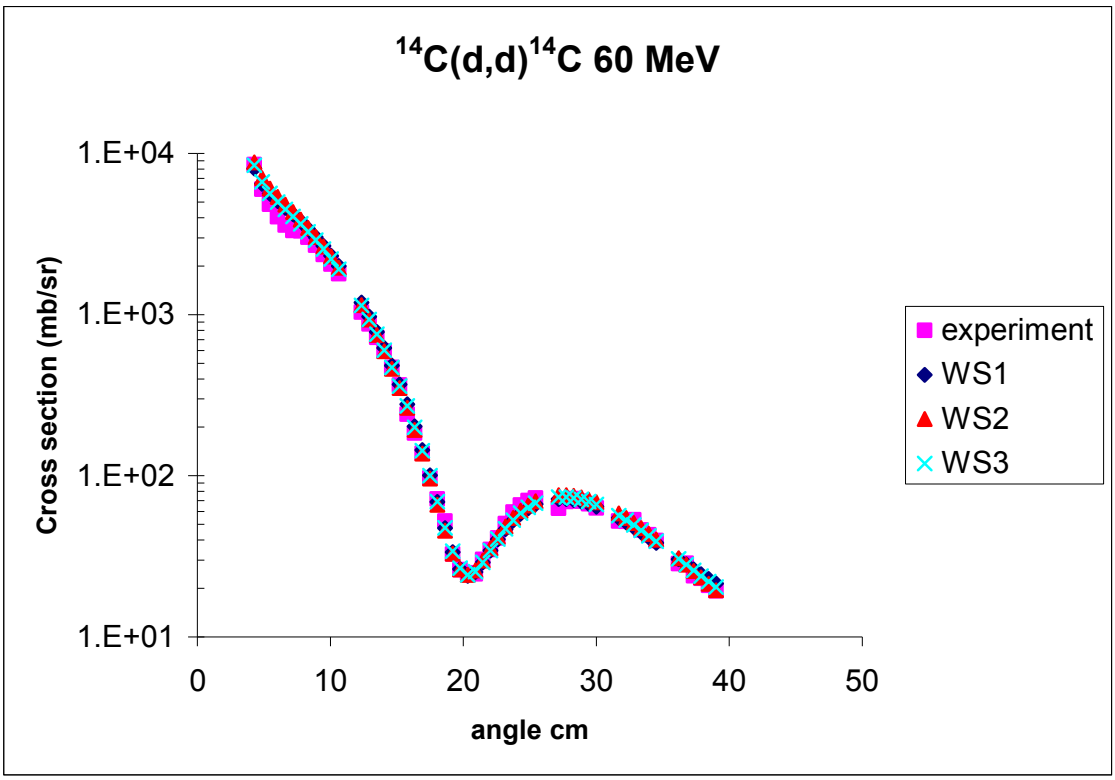

Fig. 25. Elastic angular distribution for 60 MeV deuterons on ^{14}C.

Table 4. Summary of optical potentials for elastic scattering of 60 MeV deuterons on ^{14}C.

	V (MeV)	W (MeV)	r_v (fm)	r_w (fm)	a_v (fm)	a_w (fm)	χ^2
WS1	151	8.05	1.36	4.59	0.920	0.913	1.19
WS2	274	17.3	1.79	2.54	0.729	1.30	1.437
WS3	376	3.88	1.24	5.56	0.739	0.861	0.871

The (*d*,*p*) on ^{14}C was calculated using the ADWA in the same manner as was described in the previous section (Fig. 26). In order to attempt to fix the single particle ANC and thus the neutron binding geometry, the angular distribution was calculated for r_0=0.9 to 2.0 fm, while the diffuseness was kept fixed at a=0.65 fm. The potential depth was adjusted at each point to reproduce correctly the binding energy. In order to compare with the experiment, the calculated differential cross section was taken at θ_{CM}=4.1°, which corresponds to the lowest measured angle and for each point was divided by the square of the SPANC to get the function R_{DW} of Eq. (2.53). This was compared with R_{exp} and for the transfer to the ground state is shown in Fig. 27. Dependence on the interior is clearly very weak, particularly in comparison with the experimental uncertainty. Because of this, the method of [8] to fix the geometry and remove this ambiguity in the SF can not be applied for this case. The error bars on the theory points reflect an assumed 10% uncertainty due to the ambiguity of the optical potential. Uncertainty for the experimental value of R is from both the ANC (8%) and the measurement of the cross section at the lowest angle (14%).

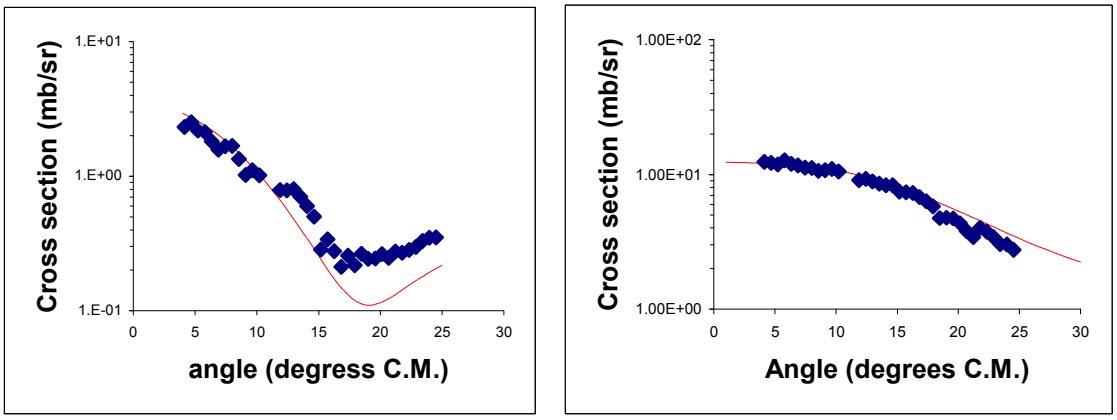

Fig. 26. On the left is the angular distribution for transfer to the ground state (blue) and the ADWA calculation (red), the same is shown on the right for transfer to the $d_{5/2}$ excited state.

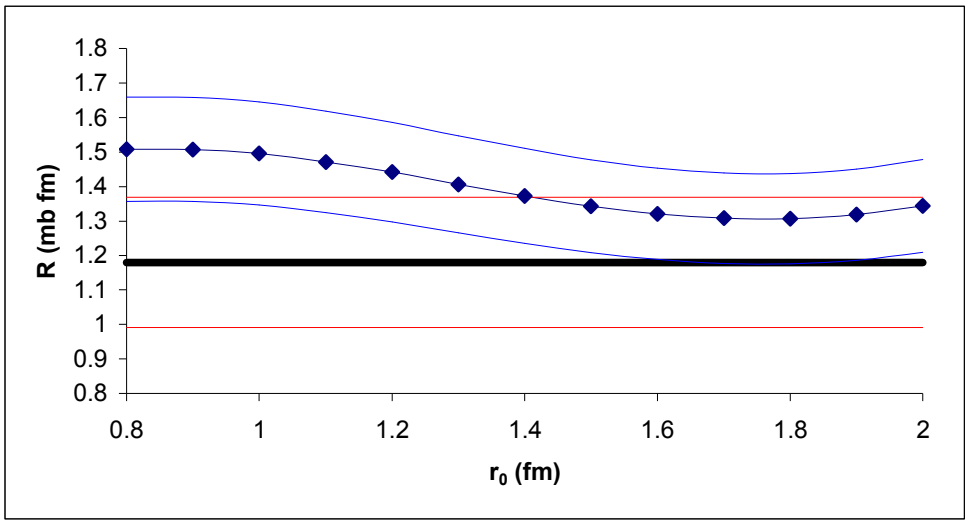

Fig. 27. Calculated points are the blue diamonds. The experimental value is the black line with the bounds of the uncertainty indicated by the red lines. The uncertainty in the calculation due to optical potential ambiguity is taken to be 10% and is indicated by the blue lines.

Given the weak dependence on the interior observed, the ANC for the ground state was determined. The value was found to be $C^2_{2s_{1/2}} = 1.76 \pm 0.29$ fm^{-1}. Uncertainties were as follows: 10% target thickness/composition, 5% data extraction, 3% normalization to the number of incident deuterons, 5% statistics, and 10% systematic uncertainty in the calculations, giving an overall uncertainty of 16%. This value was lower than those from the inverse kinematics (*d*,*p*) and the HI transfer experiment, which could be due to unaccounted contributions of other reaction channels that might be more significant at this higher energy, however it agrees within the uncertainty.

The dependence of $C^2_{2s_{1/2}}$ on the single particle ANC is shown in Fig. 28. As would be expected based the results in Fig. 27, the dependence is rather weak, which is indicative of a peripheral reaction.

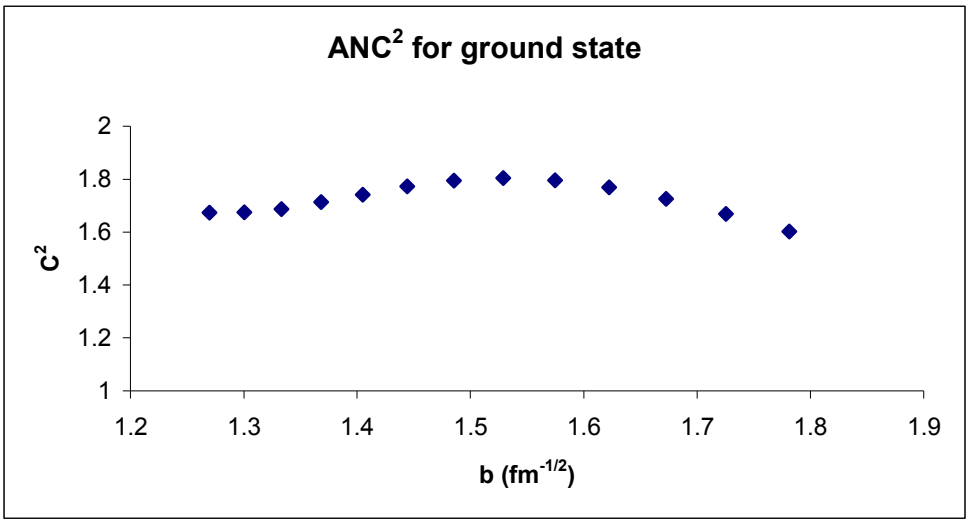

Fig. 28. C^2 for the ground state as a function of the SPANC. Uncertainty in the ANC is 16%, which is larger than the variation.

The same method to calculate R_{DW} was applied to the case of transfer to the first excited state and the result is shown in Fig. 29. In this figure the R_{exp} is the measured cross section at the smallest angle (4.1° C.M.) and the uncertainty (indicated by the red lines) corresponds to the uncertainty in C^2 (13%) extracted from the HI transfer and inverse kinematics measurements and in the measurement of the cross section at that point (12% - this point had ~3% statistical uncertainty, other sources of uncertainty were as stated above for the ground state). The dependence of R_{DW} on r_0 for the $d_{5/2}$ excited state is stronger than for the ground state and from this an upper limit on the SPANC can be set. Assuming a 10% uncertainty in the calculation due to optical potential ambiguity, Fig. 29 shows an upper limit of r_0 of ~1.15 fm, which corresponds to $b^2 = 4.01 \cdot 10^{-3}$ fm^{-1}. From the relation

$$SF_{nlj} = \frac{C^2_{nlj}}{b^2_{nlj}} \tag{4.11}$$

one obtains a lower limit of SF=1.05. No attempt was made to set an upper limit as the lowest point in R_{DW} which was calculated corresponds to r_0=0.8 fm, which is already quite low and going further would not be physically meaningful.

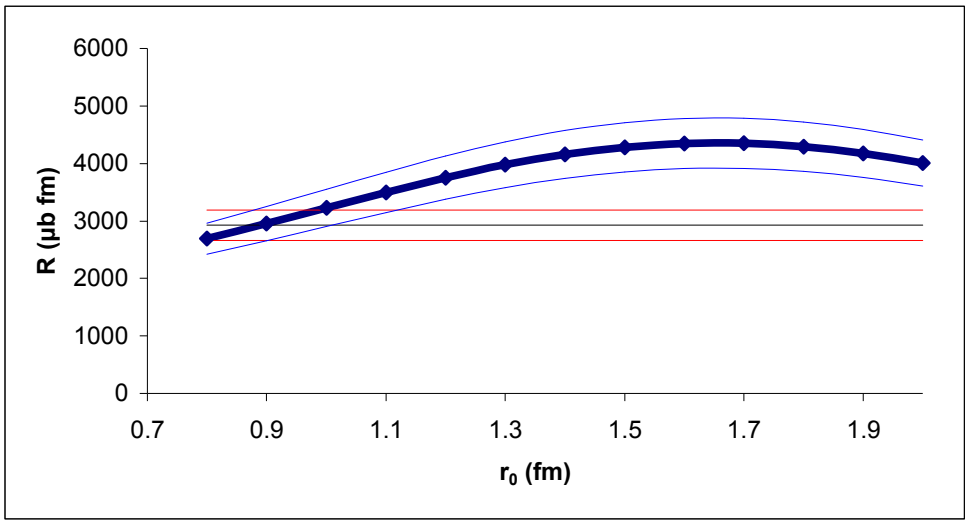

Fig. 29. R_{DW} (blue dots) and R_{exp} (black line) for transfer to the $d_{5/2}$ first excited state. The uncertainty in the calculation due to systematic uncertainties is taken to be 10% and is shown by the thin blue lines.

C. Summary of ANCs

The average value weighted for the uncertainty for the three measurements for ground state is $C^2_{2s_{1/2}} = 1.96 \pm 0.16$ fm^{-1} and for the two measurements for the first excited state is $C^2_{1d_{5/2}} = (4.23 \pm .038) \cdot 10^{-3}$ fm^{-1}. The value for transfer to the ground state is not in agreement with the value of $C^2_{2s1/2} = 1.64 \pm 0.03$ fm^{-1} found from the analysis [13] of a Coulomb dissociation experiment at 68 MeV/nucleon [24]. In [13] a comparison of a calculated excitation function with that which was measured in [24] was used to find χ^2 as a quadratic function of the ANC. The ANC at the minimum of this function was taken to be the accepted value and the uncertainty was the variation of the ANC corresponding to χ^2_{min} + 1. An uncertainty determined in this manner may be underestimated because systematic uncertainties in the experiment are not taken into account. The ANCs found from the different measurements in this work are summarized along with the average values in Table 5.

Table 5. Summary of ANCs found in the different measurements.

experiment	$C^2_{2s_{1/2}}$ (fm^{-1})	$C^2_{1d_{5/2}}$ (fm^{-1})
HI transfer	2.09±0.29	(4.48±0.58)·10^{-3}
TECSA d(^{14}C,p)^{15}C	2.01±0.24	(4.06±0.49) ·10^{-3}
60 MeV (d,p)	1.76±0.29	
average	**1.96±0.16**	**(4.23±0.38) ·10^{-3}**

An analysis of nuclear breakup measurements of ^{15}C at about 60 MeV/nucleon [49], [50] found the $C^2_{2s1/2} = 1.48 \pm 0.18$ fm^{-1} [11], which is also substantially lower than the value found here. A recent analysis of older low energy (14 MeV) ^{14}C(*d*,*p*) data [12] found $C^2_{2s1/2} = 2.14$ fm^{-1} using a similar ADWA calculation method to the one used here. The similarity of the ANCs from transfer reactions both in this work and in [12] and their apparent disagreement with the Coulomb disassociation and breakup measurements is interesting and might be indicative of the inadequacy of the current methods of transfer calculations to handle exotic, loosely bound nuclei. This possibility was explored in the analysis of a recent measurement of ^{14}C(*d*,*p*) at E_d=17 MeV made at the Nuclear Physics Institute of the Czech Academy of Sciences [14], however the ANC^2 for the ground state of ^{15}C determined using an ADWA calculation was found to be 1.64±0.26 fm^{-1}, which is consistent with the Coulomb disassociation analysis of [13]. If a larger uncertainty is considered for the value from Ref. [13] such as 15%, then there would not be a disagreement with the value found in this work. A summary of the ANCs is given in Table 6.

Table 6. Comparison of ANC values from previous determinations.

	$C^2_{2s_{1/2}}$ (fm^{-1})	$C^2_{1d_{5/2}}$ (fm^{-1})
Ref. [11]	1.48±0.18	
Ref. [10]	1.89±0.11	
Ref. [12]	2.14	
Ref. [13]	1.64±0.03	
Ref. [14]	1.64±0.26	3.55±0.43
This work	1.96±0.16	4.23±0.38

CHAPTER V

ASTROPHYSICAL $^{14}C(n,\gamma)^{15}C$ CROSS SECTION AND CONCLUSION

A. The (n,γ) calculation

The radiative neutron capture rates for $^{14}C(n,\gamma)^{15}C$ have been calculated using the code RADCAP [51] and the ANCs that were found in the previous chapter. At astrophysical energies only the first two states, the $2s_{1/2}$ ground state and the 740 keV $1d_{5/2}$ first excited state, contribute to the neutron capture cross section. The next state at 3.1 MeV and ~ 40 keV in width is too high to contribute [26]. S-wave neutron capture is not significant for the $^{14}C(n,\gamma)$ reaction due to parity conservation [22]. ^{14}C has $J^{\pi}=0^{+}$ and coupled with an s-wave neutron would give a system with $J^{\pi}=1/2^{+}$. Because the ground and first excited states in ^{15}C are $J^{\pi}=1/2^{+}$ and $J^{\pi}=5/2^{+}$, respectively this only allows for weak M1 and E2 transitions. Alternatively, a p-wave neutron would give the $^{14}C+n$ system $J^{\pi}=1/2^{-}$ or $3/2^{-}$, which would then be able to allow E1 transitions and thus a much higher cross section. For the first excited state E2 transitions should also be taken into account [22].

RADCAP solves the Schrödinger equation for the relative motion of the core (in this case ^{14}C) and the captured particle (in this case a neutron), using a potential chosen by the user. Two options for potentials are the user-defined potential of the Wood-Saxon form with central nuclear, spin orbit and, in the case of charged particle capture, Coulomb terms or a semi-microscopic calculated potential using the M3Y interaction. In all the calculations presented here the first option, the phenomenological WS potential, was used. RADCAP uses the potential entered by the user to calculate the bound state wave function to be used as input for the capture calculation, and saves this function in a file for later use. With the bound state wave function calculated, the program is run again, this time to calculate the capture reaction. The direct radiative capture cross section is found via detailed balance from the photo-absorption cross section. Again, the potential used for the core plus captured particle interaction is specified by the user, and the equation of relative motion is solved, this time for the continuum state over an energy range dictated by the user. To calculate the photo-absorption cross section, the continuum wave function is used to calculate the matrix element for the photo-transition and, in turn, the total multipole strength by summing the multipole strength over the partial waves that the user

specifies. The total multipole strength is then used to calculate the photo-absorption cross section and, from that, the capture cross section.

The average single particle spectroscopic factors from the three measurements presented in the last chapter were 1.0 and 0.99 for the ground state and first excited state respectively, which are consistent with a N=8 closed shell and a neutron in a sd-shell single particle state. The neutron binding potential used was of the WS form with the real potential depth adjusted to reproduce the neutron binding energy for each state. The neutron separation energy for ^{15}C is 1.218 MeV. The binding potential parameters were, for the ground state, V_0=-54.71 MeV, r=2.8922 fm, a=0.60 fm and V_{SO}=-9.30 MeV (using the SO convention described in [51]). The same geometry was used for the real and SO parts of the potential. The real depth was V_0=-54.11 MeV for the first excited state.

The cross section divided by the square root of the energy is given in Fig. 30 for both capture to the ground state and the first excited state. The capture to the first excited state accounts for about 4% of the total (only the two states are considered). The sum of the two states is shown along with the recent direct measurement of Reifarth *et al.* [19] in Fig. 31.

The calculated value for the cross section for capture to the ground state at 23 keV was σ_{gs}(23 keV)=5.1±0.4 μb and to the first excited state was σ_{exc}(23 keV)=0.19±0.02 μb. The total cross section at 23 keV was found to be σ(23 keV)=5.3±0.5, which is in good agreement with the most recent direct measurement [19].

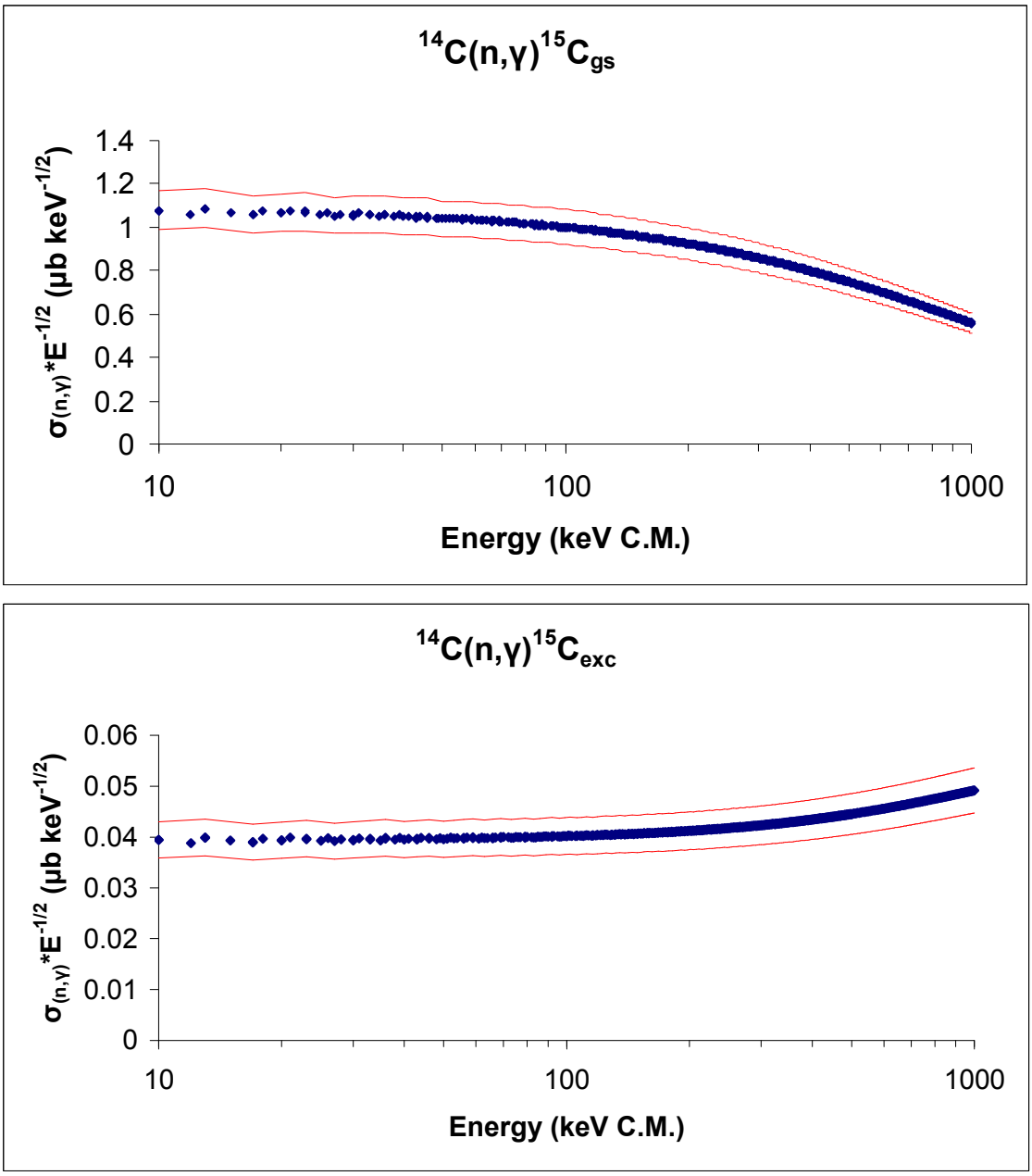

Fig. 30. Top shows the cross section divided by the square root of the energy for capture to the ground state. The bottom shows the same for the first excited state.

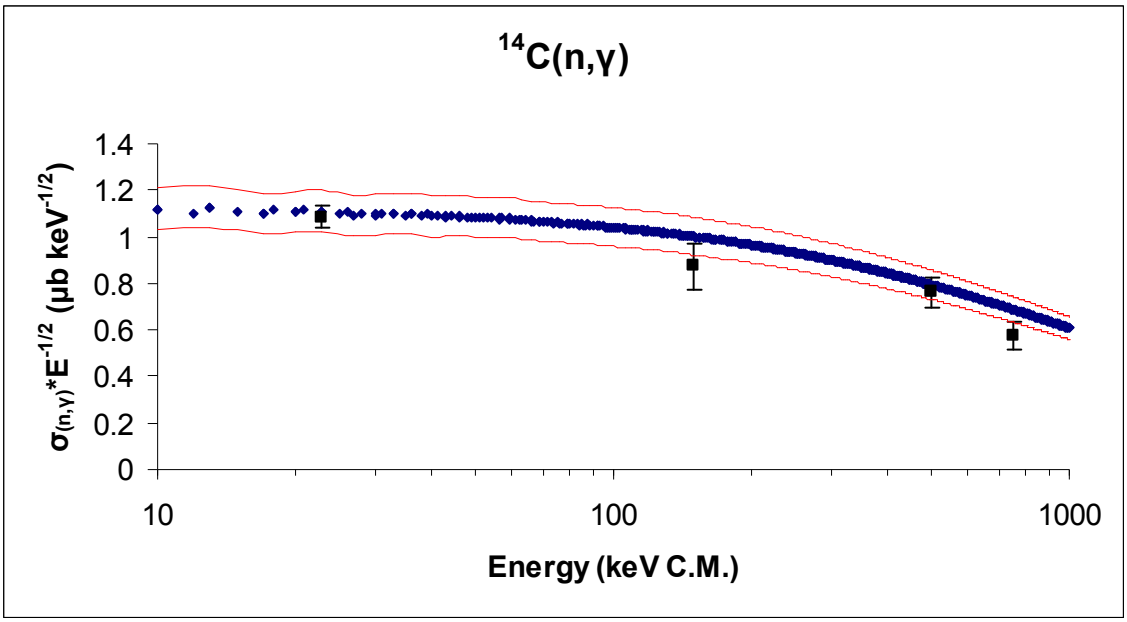

Fig. 31. Calculated cross section (sum of capture to gs and 1st exc. state, blue dots with red uncertainty) compared with Ref. [19] (black squares).

B. Conclusion

The ANCs for $^{15}C \leftrightarrow {}^{14}C+n$ were measured in three separate experiments and the values $C^2_{2s1/2} = 1.98 \pm 0.15$ fm^{-1} and $C^2_{1d5/2} = (4.27 \pm 0.43) \cdot 10^{-3}$ fm^{-1} were obtained. These results are in reasonable agreement with previous values ([13],[12]), especially when one considers that the uncertainty quoted in [13] is unrealistically low. The values obtained here are also in good agreement with the recent work described in Ref. [14].

We were unsuccessful in our attempt to apply the method of [8] to obtain a less ambiguous SF for the ground state of ^{15}C as a result of a weak dependence on the interior for the higher energy (*d*,*p*) reaction that was measured. Because of the momentum mismatch in the entrance and exit channels and the resulting small cross section at higher energies, it is unlikely that this reaction could be measured at a less peripheral energy using the same technique. Also, depending on the energy necessary to achieve an adequate interior contribution, moving to a significantly higher energy may bring into question the validity of the assumptions inherent in the DWBA. A stronger dependence on the SPANC was observed for transfer to the $d_{5/2}$ first

excited state of ^{15}C and an upper limit on SPANC^2 of 4.01 fm^{-1} and thus a lower limit on the SF of 1.05 was obtained. The dependence on the SPANC for the $d_{5/2}$ state was still rather weak and if the ANC for the first excited state were found to be slightly lower than determined here, as was the case in [14], and the comparison of R_{DW} to R_{exp} were repeated using this ANC, no limit could be assigned.

This method might be more useful for states with higher *l*, as the shape of the binding potential has a more significant effect at larger radii for such states. However, as shown here, even for a relatively high deuteron energy and a loosely bound halo nucleus, the transfer to an s state does not have a strong enough dependence on the interior. In [8] the example of (*d*,*p*) on ^{208}Pb was given as one such reaction with a higher l that would have a strong dependence on the interior. With this stronger interior dependence, ^{208}Pb(d,p) is an example of the kind of reaction where this method would work better.

Recently [52], the use of transfer reaction rates in the determination of SFs was shown to be impossible in the context of future exact many-body theory. In such an exact calculation the SF is dependent on the NN and many-body potentials of which there are an infinite number that will produce the same asymptotic behavior and thus the same ANCs and reaction rates. Even $(e,e'p)$ reactions which probe deep into the nuclear interior are subject to ambiguities as a result of short-range correlations which can affect the overlap function (and thus the SF) but do not change the reaction amplitude (the observable in those reactions). This information reiterates the point that the SF extracted from normalizing a DWBA calculation to a reaction amplitude is a single particle SF that relates the single particle bound state wave function of the transferred nucleon to the overlap function of the initial and final states. The vast majority of the amplitudes for both the overlap function and the single particle bound state wave function lie deep within the nuclear interior and are not probed in transfer reactions. These single particle SFs are certainly useful but must be taken within the context of the model dependencies with which they were extracted.

The method tested in this work seeks to reduce the model dependency of extracted SFs and has been experimentally demonstrated to have at least limited success, in this case for the excited state of ^{15}C. However, the difficulty of getting a strong enough dependency on the nuclear interior was also demonstrated and this must be carefully considered in any future attempts to utilize this method. Transfer reactions remain a key tool in the exploration of the

structure of exotic nuclei and methods to better utilize the information from these reactions in this exploration is important and should be pursued.

REFERENCES

[1] E. Rutherford, Philosophical Magazine **6,** 21 (1911).

[2] D.C. Cassidy, G. Holton, and J. Rutherford, *Understanding Physics* (Springer-Verlag, New York, 2002).

[3] N. Bohr, Nature **137**, 3461 (1936).

[4] F.S. Dietrich and J.E. Escher, Nucl. Phys. **A787**, 237 (2007).

[5] S.T. Butler, R. Soc. Lond. **A208**, 559 (1951).

[6] A.M. Mukhamedzhanov, C Gagliardi, and R. Tribble. Phys. Rev. C **63**, 024612 (2001).

[7] S.A. Goncharov, J. Dobesh, E.I. Dolinskii, A.M. Mukhamedzhanov, and J. Ceijpek, Sov. J. Nucl. Phys. **35**, 3 (1981).

[8] A.M. Mukhamedzhanov and F.M. Nunes. Phys. Rev. C **72**, 017602 (2005).

[9] A.M. Mukhamedzhanov, H.L.Clark, C.A. Gagliardi, Y.-W. Lui, L. Trache, *et al.*, Phys. Rev. C **56**, 1302 (1997).

[10] N.K. Timofeyuk, D. Baye, P. Descouvemont, R. Kamouni, and I. J. Thompson, Phys. Rev. Lett. **96,** 162501 (2006).

[11] L. Trache, A. Azhari, F. Carstoiu, C.A. Gagliardi, A.M. Mukhamedzhanov, X.D. Tang, R.E. Tribble, and S. Zhou, Texas A&M Cyclotron Progress Report, I-16 (2002).

[12] D.Y. Pang, F.M. Nunes and A.M. Mukhamedzhanov, Phys. Rev. C **75**, 024601 (2007).

[13] N.C. Summers and F.M. Nunes, Phys. Rev. C **78**, 011601(R) (2008).

[14] A. Mukhamedzhanov, V. Burjan, M. Gulino, Z. Hons, V. Kroha, M. McCleskey, *et al.,* Phys. Rev. C., in press (2011).

[15] J.H. Applegate and C.J. Hogan, Phys. Rev. D **31**, 3037 (1985).

[16] R.A. Malaney and W.A. Fowler, Astrophys. J. **333**, 14 (1988).

[17] T. Rauscher, Phys Rev. D **75**, 068301 (2007).

[18] M. Wiescher, J. Görres, and H. Schatz, J. Phys. G: Nucl. Part. Phys. **25**, R133 (1999).

[19] R. Reifarth, M. Heil, C. Forssen, U. Besserer, A. Couture, *et al.,* Phys. Rev. C **77**, 015804 (2008).

[20] M. Terasawa, K. Sumiyoshi, T. Kajino, G.J. Mathews, and I. Tanihata, Astrophys. J. **562**, 470 (2001).

[21] H. Beer, M. Wiescher, F. Käppeler, J. Görres ,and P.E. Koehler, Astrophys. J. **387**, 258 (1992).

[22] M. Wiescher, J. Görres, and F.K. Thielemann, Astrophys. J. **363**, 340 (1990).

[23] T. Kajino, G.J. Mathews, and G.M Fuller, Astrophys. J. **364**, 7 (1990).

[24] T. Nakamura, N. Fukudab, N. Aoic, H. Iwasakic, T. Kobayashi, *et al*., Nucl. Phys. **A722**, 301c (2003).

[25] T. Nakamura, N. Fukuda, N. Aoi, N. Imai, M. Ishihara, *et al.*, Phys. Rev. C **79**, 035805 (2009).

[26] A. Horvath, J. Weiner, A. Galonsky, F. Deak, Y. Higurashi, *et al*., Astrophys. J. **570**, 926 (2002).

[27] U.Datta Pramanik, T. Aumann, K. Boretzky, B.V. Carlsond, D. Cortinae, *et al.*, Phys. Lett. **B551,** 63 (2003).

[28] L. Trache, A. Azhari, H. L. Clark, C. A. Gagliardi, Y.-W. Lui, A. M. Mukhamedzhanov, and R. E. Tribble*,* Phys. Rev. C **61**, 024612 (2000).

[29] J.P. Juekenne, A. Lejeune, and C. Mahaux, Phys. Rev. C **16**, 80 (1977).

[30] D.H. Youngblood and J.D. Bronson, NIM A **361**, 37-45 (1995).

[31] D.M. Pringle, W.N. Catford, J.S. Winfield, D.G. Lewis, N.A. Jelley and K.W. Allen, NIM A **245**, 230 (1986).

[32] S. Kowalski and H.A. Enge, computer code RAYTRACE (unpublished), University of Oxford, UK (1986).

[33] B.T. Roeder, M. McCleskey, L. Trache, A.A. Alharbi, A. Banu *et al.,* NIM A **634**, 71 (2011).

[34] A. Banu, Y. Li, M. McCleskey, M. Bullough, S. Walsh, *et al.,* NIM A **593**, 399 (2008).

[35] S.L. Thomas, T. Davinson, and A.C. Shotter, NIM A **288**, 212 (1990).

[36] O.B. Tarasov and D. Bazin, NIM B **266**, 4457 (2008).

[37] F. Carstoiu, computer code OPTIMINIX (unpublished), Institute of Physics and Nuclear Engineering, Bucharest, Romania (1996).

[38] M. Rhoades-Brown, S. Pieper, and M. Macfarlane, computer code PTOLEMY, Argonne National Lab Report ANL-76-11-rev-1 (1978).

[39] R. Brun and F. Rademakers, NIM A **389**, 81 (1997).

[40] T. Al-Abdullah, F. Carstoiu, X. Chen, H. L. Clark, C. Fu *et al.,* Phys. Rev. C **81**, 035802 (2010).

[41] R.L. Varner, Physics Reports **201** (2), 57 (1991).

[42] R.C. Johnson and P.J.R. Soper, Phys. Rev. C **1**, 976 (1970).

[43] R.C. Johnson and P.C. Tandy, Nucl. Phys. **A235,** 56 (1974).

[44] G.L. Wales and R.C. Johnson, Nucl. Phys. **A274,** 168 (1976).

[45] N.B. Nguyen, F.M. Nunes and R.C. Johnson, Phys. Rev. C **82**, 014611 (2010).

[46] R.V. Reid, Ann. of Phys. **50**, 411 (1968).

[47] I.J. Thompson, Comput. Phys. Rep. **7**, 167 (1988).

[48] S.M. El-Kadi, C. E. Nelson, F. O. Purser, R. L. Walter, A. Beyerle, C. R. Gould, and L. W. Seagondolla, Nucl. Phys. **A390**, 509 (1982).

[49] V. Maddalena, T. Aumann, D. Bazin, B.A. Brown, J.A. Caggiano *et al.,* Nucl. Phys. **A682**, 332c (2001).

[50] E. Sauvan, F. Carstoiu, N. A. Orr, J. C. Angélique, W. N. Catford *et al.,* Phys. Lett. B **491**, 1 (2000).

[51] C.A. Bertulani, Comput. Phys. Commun. **156**, 123 (2003).

[52] A.M. Mukhamedzhanov and A.S. Kadyrov, Phys. Rev. C **82,** 051601(R) (2010).

VITA

Matthew Edgar McCleskey received his Ph.D. (2011) and his B.S. (2006) from Texas A&M University. He graduated high school from the Texas Academy of Mathematics and Science at the University of North Texas (2003). He has worked as a graduate research assistant (2006-2011) and student worker (2003-2006) at the Texas A&M Cyclotron Institute and previously as a student worker (2002-2003) at the Ion Beam Modification and Analysis Laboratory at the University of North Texas.

His address is Cyclotron Institute, Texas A&M University MS 3366, College Station, TX 77803. His email is matthewmccleskey@tamu.edu.